Cooling of Highly Concentrated Photovoltaic Cells with Confined Jet Impingement by Introducing Channel Configurations

Abhishek Gupta [a], Sandesh S. Chougule [b c], Sandip K. Saha [a]

[a] Department of Mechanical Engineering, Indian Institute of Technology Bombay, Mumbai, 400076, India

[b] Clean Energy Processes (CEP) Laboratory, Department of Chemical Engineering, Imperial College London, London, SW7 2AZ, United Kingdom

[c] Solar Flow Ltd., London, SW11 3BQ, United Kingdom

N.B.: This is the ACCEPTED MANUSCRIPT version of this article. The final, published version of the article can be found at: https://doi.org/10.1016/j.renene.2024.121600

Abstract

Appropriate cooling techniques are required to be integrated into highly concentrated photovoltaic cells to maintain the surface of the photovoltaic cell at a uniform temperature. This study focuses on cooling photovoltaic cells with confined jet impingement to reduce non-uniform temperature distribution and thermal and bending stresses to avoid hotspots and current mismatching problems, thereby improving the cell electrical efficiency. Channels are formed in an aluminium heat sink on the backside of solar cell layers such that the coolant strikes the heat sink surface at the centre and exits at the four corners of the module. Different designs of confined jet channel configurations are studied. The effect of the coolant mass flow rate on the hydrothermal performance of the concentrated photovoltaic thermal (CPV-T) system is examined for all channel configurations. The electrothermal performance of the CPV-T system is at its maximum with a quadrant mini-channel with a single inlet. The net electrical power generated by the PV cell is at its maximum of 30.5 W for a mass flow rate of 50 g/min with this channel configuration. Further, the pressure loss is minimal at 163 Pa at 25 g/min, and the temperature uniformity is also maximum, with a temperature difference over the cell surface of 6.3 °C at 50 g/min. The present study will be useful in the thermal management of highly concentrated photovoltaic thermal systems and high-temperature applications.

Keywords: Highly concentrated photovoltaic cell; Channel design; Confined jet impingement; Efficiency; Exergy; Stress

* Corresponding author. Tel.: +91 22 25767392; fax: +91 22 2572 6875.
E-mail address: sandip.saha@iitb.ac.in

Nomenclature

A	Area of the solar cell (m^2)
C_p	Specific heat (J/kg·K)
CR	Concentration ratio
E	Exergy (W)
I	Direct solar irradiation (W/m^2)
G	Total concentrated solar irradiation (W/m^2)
H	Total thickness of the Germanium and copper layers (m)
h	Convective heat transfer coefficient ($W/m^2 \cdot K$)
k	Thermal conductivity (W/m·K)
$\dot{m}$	Mass flow rate (kg/min)
P	Power (W)
q	Heat generation (W/m^3)
Q	Energy (W)
T	Temperature (°C)
ΔT	Temperature difference (°C)
$\vec{V}$	Velocity vector (m/s)
V	Volume of the solar cell (m^3)

Greek symbols

μ	Viscosity of water (Pa·s)
α	Absorptivity
α_T	Thermal expansion coefficient (K^{-1})
v	Poisson ratio
β_T	Temperature coefficient of the solar cell

η	Efficiency (%)
σ	Stefan-Boltzmann constant ($W/m^2 \cdot K^4$)
σ_b	Bending stress (Pa)
σ_T	Thermal stress (Pa)
ρ	Density of water (kg/m^3)

Subscript

a	ambient
al	aluminium
cell	Solar cell
conv	convection
cu	copper
ce	ceramic
el	electrical
f	fluid
fric	frictional
Ge	Germanium
in	inlet
m	mean
opt	optical
out	outlet
rad	radiation
ref	reference
th	Thermal

Abbreviations

CPV	Concentrated photovoltaic

CJI	Confined jet impingement
HCPV	Highly concentrated photovoltaic
HCPV-T	Highly concentrated photovoltaic thermal
PV	Photovoltaic
HTC	Heat transfer coefficient
CTE	Coefficient of thermal expansion

34

35

1. Introduction

Solar energy is considered a significant renewable energy source. Solar energy has an annual potential of 1,575–49,837 exajoules (EJ), which is 1.8–58 times greater than the projected 860 EJ global energy consumption in 2040 [1, 2]. Solar energy is used to obtain electrical and thermal energy outputs by various technologies, such as photovoltaic (PV) systems, concentrated PV (CPV) systems, and solar thermal collectors. PV systems and solar thermal collectors can be integrated to obtain electrical and thermal energy outputs simultaneously. Photovoltaic thermal (PV-T) systems can be used to expand solar energy utilization by improving solar cell conversion efficiency. However, the flat plate PV-T systems are restrained for high-temperature applications since they generate heat at very low temperatures. Concentrated photovoltaic thermal (CPV-T) systems are a better alternative to overcome such problems.

A CPV-T system focuses sunlight onto a small area of high-efficiency photovoltaic material. Unlike traditional solar PV cells that generate electricity from sunlight over a large surface area, CPV systems employ lenses or mirrors to concentrate sunlight onto a smaller, more efficient solar cell. This concentration of sunlight allows for the use of high-efficiency solar cells that might be more expensive but can generate more electricity per unit area. However, CPV-T systems also face several issues despite having these advantages. High concentrations of solar radiation on photovoltaic cells lead to extremely high cell temperatures, which results in decreased cell efficiency. The amount of solar energy that is transformed into electricity is quite minimal. The remaining solar energy is translated into thermal energy, resulting in problems such as hotspots, current mismatching, and thermal fatigue. A high concentration of solar light on PV cells also results in a non-uniform distribution of temperature on the cell surface, leading to thermal stresses and lower life of PV cells. Appropriate cooling techniques need to be integrated with the CPV-T systems to sustain the high-temperature rise

and maintain a uniform temperature throughout the photovoltaic cell. Many cooling techniques have been employed in various literature, such as air-based cooling, liquid immersion, jet impingement, phase change material cooling, micro-channel cooling, thermoelectric cooling, and heat pipe cooling [3].

Theristis et al. [4] reported that passive cooling methods are not able to extract sufficient heat from HCPV-T systems. Jet impingement is an appropriate cooling method for densely packed PV cells to achieve a uniform cell temperature [5]. Many researchers have investigated both unconfined and confined jet impingement (CJI) cooling schemes for PV cells. Javidan et al. [6] found that the temperature of a PV module of dimensions of 36 cm × 27.5 cm was reduced from 63.95 °C to 33.68 °C for a solar irradiance of 1000 W/m^2 using an optimal set of parameters of multi-nozzle unconfined jet impingement cooling. The authors obtained a temperature uniformity index of approximately 0.3 °C for a nozzle number of 24, mass flow rate of 0.12 kg/s, nozzle diameter of 2 mm and nozzle-to-PV cell distance of 5. Bahaidarah et al. [7] studied the effect of the unconfined jet impingement cooling scheme on PV cells using 8 nozzles with a diameter of 5 mm and nozzle-to-plate distance of 5.3. The authors observed a temperature decrease from 69.7 °C to 36.6 °C with a temperature uniformity of 1 °C with a flow rate of 1.5 L/min for a 1000 W/m^2 solar irradiation. Zubeer et al. [8] performed an experimental and numerical study to assess the water-cooling effect on low-concentrated PV modules of dimensions 1968 mm × 990 mm. The temperature of an uncooled PV system and a low-concentrated (1-3 suns) PV system was found to be 57.5 °C and 64.1 °C, respectively, which was decreased to 36.5 °C with water jet impingement cooling with a flow rate of 3 L/min. Markal et al. [9] conducted experiments to evaluate the effect of impinging air jets, employing 6 nozzles with a nozzle-to-plate spacing of 8, on the cooling of a PV cell with dimensions of 157 mm × 145 mm. It was found that the reduction in the cell temperature was 61.5%, and the output power was improved by 13.2% with a flow rate of 300 L/min. Amanlou

et al. [10] examined the effects of air diffuser geometry and air mass flow rates on the overall performance of low-concentrated PV systems. By increasing the flow rates from 8×10^{-3} to 16×10^{-3} kg/s, the electrical, thermal, and overall efficiencies of the solar PV cell of dimensions 0.8 m ×1 m were improved by 13.5%, 22.75%, and 22.41%, respectively.

The unconfined jet impingement needs numerous nozzles to cool PV cells; however, temperature uniformity across the cell may not be ensured at high concentration ratios for densely packed PV cells. Therefore, several researchers have proposed and investigated hybrid cooling systems comprising jet impingement and multichannel cooling. Dong et al. [11] considered only the T-shaped channel to cool a PV cell of 10 mm ×10 mm with a concentration ratio of 500. The authors found a temperature uniformity of 26 °C with a coolant velocity of 0.64 m/s. Barrau et al. [12], using a numerical model, studied the effectiveness of hybrid jet impingement and microchannel cooling strategy for densely packed PV cells. The temperature uniformity of 2.01 K was obtained using a modified hybrid microchannel heat sink geometry for a flow rate of 1.8×10^{-4} m^3/s and a concentration ratio (*CR*) of 458. Abo-Zahhad et al. [13] demonstrated that the cell temperature can be reduced from 1360 °C to 65 °C with water at a mass flow rate of 50 g/min for *CR* of 1000 suns using the CJI cooling technique. The authors found the temperature uniformity of 6 °C for *CR* = 1000 for a cell size of 10 mm × 10 mm for 25 g/min. However, their study did not consider any channel in the heat sink. Tang et al. [14] studied the ultrathin micro pin-fin channel for cooling of HCPV-T system. The cell temperature was found to be 51 °C with a temperature uniformity of 3.4 °C at *CR* = 1000 at a mass flow rate of 3 kg/h. The pressure drop was 2.73 kPa for circular pin-fin and 5.29 kPa for square pin-fin design at a mass flow rate of 1.5 kg/h. Shobhy et al. [15] studied the effect of trimmed fins and microchannels on the performance of the HCPV-T system. The temperature uniformity was found to be 20.6 °C with a hybrid heat sink at a mass flow rate of 200 g/min at *CR* = 2500.

111 It can be concluded from the literature review that the temperature uniformity of highly
112 concentrated PV cells is found to be low without any cooling, which leads to problems such as
113 current mismatching, thermal hotspots, and thermal stresses. The jet impingement cooling
114 technique is an efficient way of cooling PV cells under high concentrations. Most of the
115 literature in this context is limited to unconfined jet impingement cooling, which uses several
116 nozzles to cool the PV cell. The use of an array of unconfined jet impingement nozzles for
117 cooling densely packed PV cells may not be possible due to space constraints. Therefore, a CJI
118 cooling scheme could be an attractive solution that can reduce the local hot spots on the PV
119 cell. However, few studies have been reported on the CJI cooling technique. Confined jet
120 impingement cooling combines jet impingement and an array of micro-channels. However, this
121 approach suffers from flow maldistribution in multiple micro-channels and significant pressure
122 drop across the microchannel heat sinks. Therefore, a heat sink for CJI cooling is required to
123 be designed by adopting mini-scale channels with simple inlet arrangements to dissipate high
124 heat generated in the densely packed PV cells with reduced pressure drop. By introducing jet
125 impingement at the centre of the heat sink and allowing the coolant to flow through mini-scale
126 channels, the temperature non-uniformity across the PV cell could be reduced by improved
127 convective heat transfer coefficient along the channel path. However, the heat sink channel
128 design for CJI has not been reported in the published literature. Therefore, the present study
129 aims to design a highly efficient CPV-T system using a CJI cooling technique with innovative
130 channel configurations and simplified inlet design in heat sinks with minimal energy losses.
131 The effect of different channel configurations in heat sinks on the performance and temperature
132 uniformity of the CPV-T system has been studied. A three-dimensional, steady-state model of
133 the solar PV cell with an integrated heat sink is developed using the finite volume approach.
134 The variation in coolant temperature, coolant mass flow rate, and convective heat transfer
135 coefficient along the length of the channel is investigated. Also, the effect of coolant flow rate

on the output parameters of the CPV-T system, such as electrical efficiency, thermal efficiency, electrical and thermal exergies, and thermal and bending stresses over the cell surface, are evaluated for all the channel configurations. An optimized channel configuration is proposed based on the pressure drop and net power output.

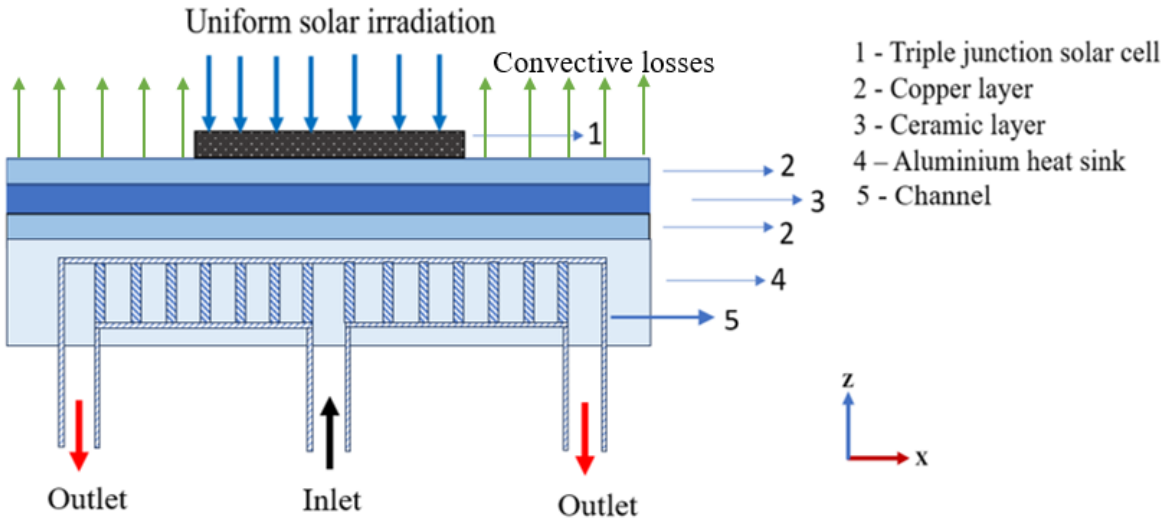
2. Model description

The HCPV-T system consists of a solar concentrator that concentrates the solar irradiation on the upper surface of the solar PV cell. The solar cell, direct bond copper assembly and heat sink designs used in the current numerical simulation study are shown in Figure 1. The solar PV cell taken for the current study is a 10×10 mm cell with an optical efficiency of 90% [16]. The PV cell has an electrical efficiency of 40.3% under CR = 1000 at a base temperature of 25 °C [16]. The solar cell is supported by a direct bond copper assembly comprising a ceramic layer and two copper layers. The dimensions of the copper and ceramic sheets are 25×25 mm. An aluminium heat sink is integrated at the bottom of the assembly to absorb the heat generated due to solar irradiation on the PV cell, which is cooled using the CJI cooling scheme. The dimensions of the heat sink are 25×25 mm with a 4 mm thickness. The coolant temperature at the heat sink inlet is considered to be 25 °C. The upper surface of the PV cell and the top copper layer are subjected to convective boundary conditions. All sides of the solar cell, board structures, and heat sink are subjected to convective boundary conditions. The thermophysical properties and dimensions of solar cell layers and heat sink are given in Tables 1 and 2, respectively.

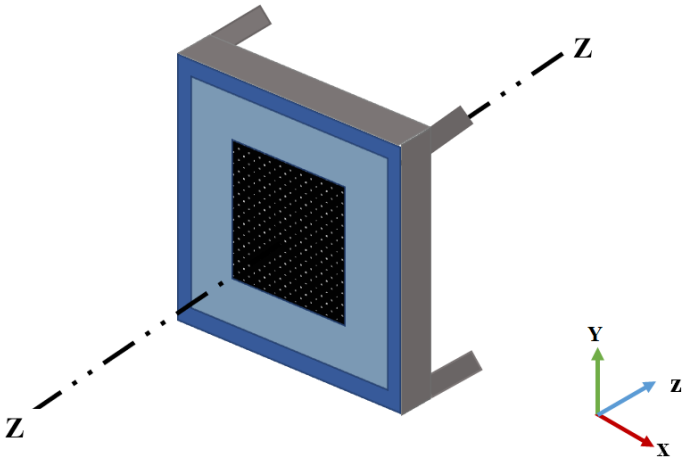
The concentrated solar radiation incidents on the PV cell surface. Solar energy is absorbed by the solar PV cell due to its high absorptivity. A small amount of solar irradiation is transformed into electrical energy by the photovoltaic effect, a function of cell temperature. The remaining portion of the absorbed solar radiation is converted into heat, resulting in an

increase in the temperature of the solar cell. The coolant in the CJI cooling technique removes the generated heat. Some portion of heat is lost by convection and radiation heat transfer to the surroundings.

In the present study, five distinct channel designs for CJI cooling are studied. The channel structures are shown in Figure 2. These channels are formed inside an aluminium heat sink to maintain a uniform temperature over the solar PV cell surface. The jet strikes the module structure at the centre and leaves at the four corners of the configurations. The channel structures are rectangular (configuration 1), circular (configuration 2), serpent (configuration 3), quadrant mini-channel with multiple inlets (configuration 4), and quadrant mini-channel with single inlet (configuration 5). The channel dimensions are chosen so that the cross-sectional area and the channel length remain constant. In the case of a rectangular channel, the channel cross-section is 1 mm × 2 mm, and the number of passes is 6. The outlets are located at 2 mm from the heat sink edges. The inlet and outlets have a rectangular cross-section of 1 mm × 1 mm. Channel configurations 4 and 5 are studied to compare the effect of the number of inlets on the performance of the HCPV-T system. The coolant is considered as water for this study.

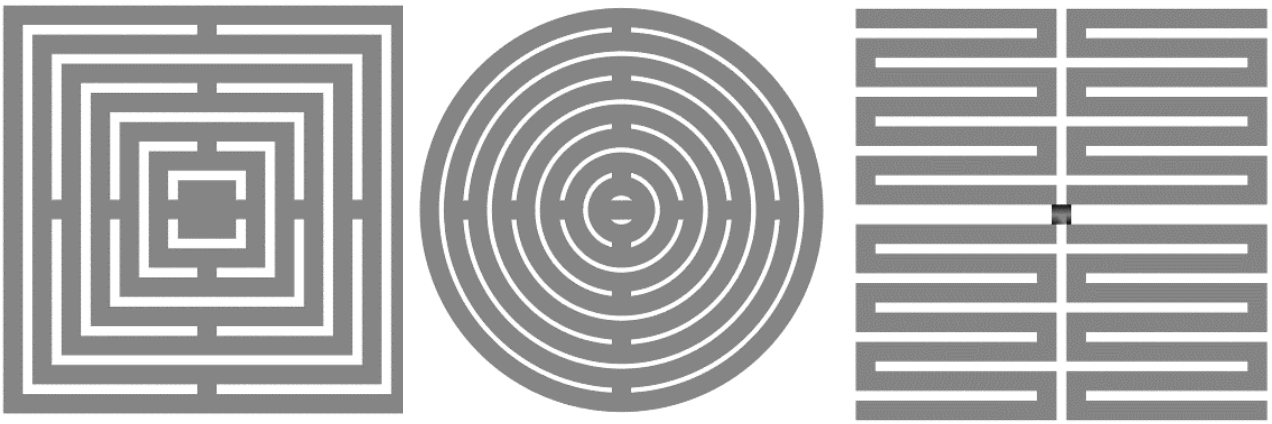


(a)

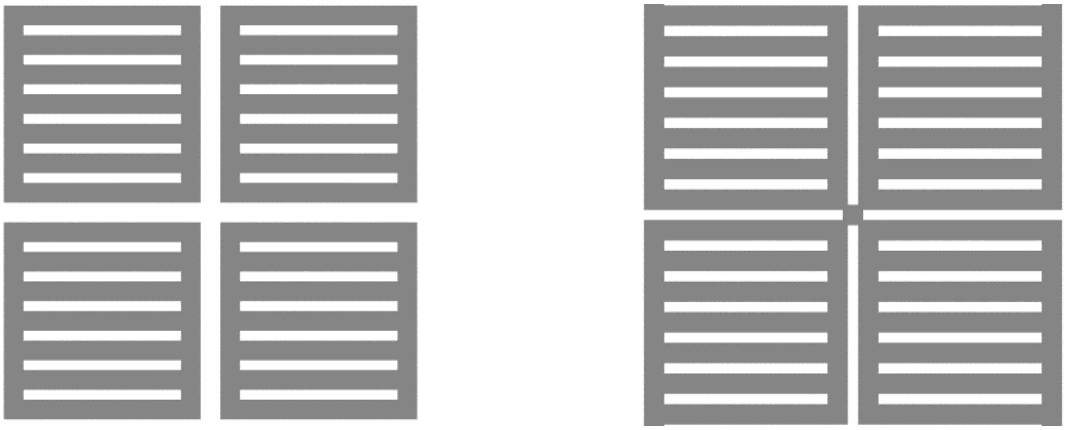


(b)

Figure 1: (a) Solar cell layers and (b) isometric view of jet impingement channel configuration



(a) (b) (c)



(d) (e)

Figure 2. Channel structures: (a) channel configuration 1, (b) channel configuration 2, (c) channel configuration 3, (d) channel configuration 4 and (e) channel configuration 5

Table 1: Thermophysical properties of solar cell, direct bond copper assembly and heat sink [17]

Layer	**Thermal conductivity (k) (W/m·K)**	**Specific heat (C_p) (J/kg·K)**	**Density (ρ) (kg/m^3)**	**Emissivity (ε)**
Germanium	60	320	5323	0.9
Copper-1	400	385	8700	0.05
Ceramic	30	900	3900	0.75
Aluminium	202.6	871	2719	0.9
Coolant fluid (water)	0.6	4182	998	-

Table 2: Dimension of solar cell, direct bond copper assembly and heat sink

Layer	**Thickness (mm)**	**Length (mm)**	**Width (mm)**
Germanium	0.19	10	10
Copper-1 and 2	0.25	25	25
Ceramic	0.32	25	25
Aluminium heat sink	4	25	25

3. Mathematical formulation

A three-dimensional configuration of the solar cell, copper and ceramic structures, and aluminium heat sink are considered for studying steady-state hydrothermal performance. In the numerical model, it is assumed that a uniform solar radiation distribution exists over the surface

194 of the cell. The flow of the coolant in the channels is assumed to be steady and incompressible.
195 The maximum Reynolds number based on the hydraulic diameter of the channel cross-section
196 is 830, which is in the laminar regime. The fluid is considered as Newtonian. The thermo-
197 physical properties are taken as isotropic and temperature-independent. A heat source term is
198 included in the energy equation since heat generation is inside the solar PV cell material, which
199 is a function of cell temperature and electrical efficiency.

200 **A. For solar cell layers:**

201 A generalized heat conduction equation for the layers of the PV cell is as follows [18]:

$$k_i \nabla^2 T_i + q_i = 0 \tag{1}$$

202 where, k_i denotes the thermal conductivity of the i^{th} layer. In all layers except the Ge layer, the
203 heat generation, q_i is set to zero. The heat generated due to solar radiation absorption in the Ge
204 layer is estimated as [18]:

$$q_{Ge} = \frac{(1 - \eta_{cell}) \cdot G \cdot \alpha_{Ge} \cdot A}{V} \tag{2}$$

205 where, G represents the net concentrated solar irradiation, α is the absorptivity of the solar PV
206 cell. The surface area and volume of the solar PV cell are represented by A and V, respectively.
207 η_{cell} denotes the electrical efficiency of the cell.

208 The net concentrated solar irradiation is a function of the optical efficiency (η_{opt}) and
209 the concentration ratio (CR) of the solar PV cell, which is given as,

$$G = I \cdot CR \cdot \eta_{opt} \tag{3}$$

210 where, I is the solar irradiation falling on the solar cell.

211 The solar PV cell efficiency, η_{cell} depends on its operating temperature. The cell
212 efficiency is reduced with the increasing temperature of the solar cell. The term (1-η_{cell})
213 signifies the amount of absorbed solar irradiance that is translated into heat. This heat has to be
214 dissipated or absorbed by the coolants to keep the cell temperature low. η_{cell} of the PV cell is
215 expressed the following equation:

$$\eta_{cell} = \eta_{ref} - \beta_T(T_{cell} - T_{ref}) \quad (4)$$

where, cell reference efficiency η_{ref} is taken as 40.3% at reference temperature T_{ref} = 298 K and CR = 1000, and β_T is the thermal coefficient and is considered as 0.047% [16].

B. For flow and heat transfer through jet impingement:

Continuity equation:

$$\rho_f \nabla(\vec{V}) = 0 \quad (5)$$

Momentum equation:

$$\rho_f(\vec{V}.\nabla\vec{V}) = -\nabla P + \mu \nabla^2 \vec{V} \quad (6)$$

Energy equation:

$$\rho_f C_{p,f}(\vec{V}.\nabla T) = k_f \nabla^2 T \quad (7)$$

where, ρ_f and μ are the coolant density and coolant viscosity, and k_f represents the thermal conductivity of the coolant. $\vec{V}$ is coolant velocity, and P is the pressure.

3.1 Calculation of electrical and thermal energies:

The total electric power, frictional power, and net electric power can be obtained as [19]:

$$P_{el} = \eta_{cell} \cdot G \cdot \alpha_{Ge} \cdot A \quad (8)$$

$$P_{fric} = \frac{\dot{m}}{\rho_f}\Delta P \quad (9)$$

where, ΔP denotes the pressure drop across the heat sink.

$$P_{net} = P_{el} - P_{fric} \quad (10)$$

The thermal power, Q_{th}, gained by the coolant from the CPV-T system is expressed as [20],

$$Q_{th} = \dot{m} C_{p,f}(T_{f,out} - T_{f,in}) \quad (11)$$

where, $T_{f,out}$ and $T_{f,in}$ are the temperatures of the coolant at the outlet and inlet, respectively.

The thermal efficiency of the CPV-T system is calculated as,

$$\eta_{th} = \frac{Q_{th}}{I \cdot CR \cdot \eta_{opt} \cdot A} \quad (12)$$

3.2 Calculation of electrical and thermal exergies

Electrical energy can be utilized completely; hence, the net electrical power, accounting for the difference between the electrical energy produced and the frictional power loss, is considered as electrical exergy. However, the thermal exergy is associated with the temperature at which the thermal energy is obtained. The thermal exergy can be determined as [21],

$$E_{th} = \dot{m}_f C_f (T_{f,out} - T_{f,in}) \left(1 - \frac{T_o}{T_m}\right) \quad (13)$$

where, T_m is the logarithmic mean temperature difference (LMTD) and is obtained using:

$$T_m = \frac{(T_{f,out} - T_{f,in})}{\ln\left(\frac{T_{f,out}}{T_{f,in}}\right)} \quad (14)$$

In equation (13), T_o is the reference temperature and is equal to 25 °C.

3.3 Stress analysis

The thermal expansion coefficients are different for the Germanium and copper layers, which are attached together. Hence, the thermal stresses exist because of the temperature difference. The thermal stress on the solar cell can be determined as [22,23]:

$$\sigma_T = E_{Ge} \cdot \Delta\alpha_T \cdot \frac{(T_R - T)}{(1 - \nu_{Ge})} \quad (15)$$

and,

$$\Delta\alpha_T = \alpha_{T,Ge} - \alpha_{T,Cu} \quad (16)$$

where, $\alpha_{T,Ge}$ and $\alpha_{T,Cu}$ are the thermal expansion coefficients of Germanium and copper, respectively. E_{Ge} is Young's modulus for the Germanium layer. T_R is the reference temperature and is equal to 25 °C. ν_{Ge} is the Poisson ratio for the Germanium layer. The values are tabulated in Table 3.

Table 3: Properties of Germanium and copper layer [24]

$\alpha_{T,Ge}$ (K^{-1})	$\alpha_{T,Cu}$ (K^{-1})	E_{Ge} (GPa)	ν_{Ge}

6.1×10^{-6}	17×10^{-6}	102.7	0.28

The coefficient of thermal expansion of the copper layer is higher than the Germanium layer. This results in tensile stress in the Ge cell layer and compressive stress in the Cu layer. Since there is no slip between the Germanium and copper layer, the layers behave like beams capable of axial and bending deformations. The curvature of the bent structure can be determined as:

$$\Gamma = \frac{1}{R} = \frac{\left(\alpha_{T,Cu} - \alpha_{T,Ge}\right)\Delta T}{\frac{H}{2} + \frac{2(E_{Ge}I_{Ge} + E_{cu}I_{cu})}{h}\left(\frac{1}{w_{cu}t_{cu}E_{cu}} + \frac{1}{w_{Ge}t_{Ge}E_{Ge}}\right)} \quad (17)$$

where, ΔT is the difference in temperature of the Ge cell with respect to the reference temperature. I_{Ge} and I_{cu} are the moment of inertia of the Ge and Cu layers, respectively. t_{Ge} and t_{cu} are the thickness of the Ge and Cu layers, respectively. H is the summation of the thickness of the Ge and Cu layers. w_{Ge} and w_{cu} are the widths of the Ge and Cu layers, respectively. The bending stress in the Ge layer can be determined using the bending equation.

$$\frac{\sigma_b}{y} = \frac{M}{I} = \frac{E}{R} \quad (18)$$

where, σ_b is the bending stress generated in the Ge layer. M is the bending moment, and R is the radius of curvature of the Ge layer.

3.4 Boundary conditions

The top layer of the concentrated PV system is subjected to mixed convection and radiation heat loss boundary conditions. All side walls of the CPV-T system are given convection boundary conditions. For the coolant, inlet jets are given uniform temperature and normal velocity boundary conditions, and at the outlet, zero-gauge pressure boundary condition is given. For the upper surface of the Ge cell and Cu layer:

$$-k_{Ge}\frac{\partial T_{Ge}}{\partial z} = q_{rad,Ge\to S} + q_{conv,Ge\to a} \quad (19)$$

$$-k_{cu}\frac{\partial T_{cu}}{\partial z} = q_{rad,cu\to S} + q_{conv,cu\to a} \quad (20)$$

where, $q_{rad,Ge\to S}$ is the radiative heat loss from the Ge cell layer to the sky and $q_{conv,Ge\to a}$ is the convective heat loss from the Ge cell layer to the ambient. The convective heat loss from the Ge cell layer to the ambient can be calculated employing the following correlations [17]:

$$q_{conv,Ge\to a} = h_{conv,wind}(T_{Ge} - T_a) \quad (21)$$

$$h_{conv,wind} = 5.82 + 4.07V_{wind} \quad (22)$$

where, T_a is the ambient temperature, T_{Ge} is the temperature of the Germanium cell, V_{wind} is the wind velocity, and $h_{conv,wind}$ is the convective HTC.

Radiation heat loss to the sky can be calculated by adopting the following expression [17]:

$$q_{rad,Ge\to S} = \sigma\epsilon_{Ge}(T_{Ge}^4 - T_s^4) \quad (23)$$

$$T_s = 0.0522T_a^{1.5} \quad (24)$$

where, ε_{Ge} is the emissivity of Ge, T_s denotes the sky temperature in Kelvin.

At the junctions between solar cell, DBC assembly and heat sink, thermally coupled boundary conditions are given.

$$-k_m\nabla T_m = -k_n\nabla T_n \; and \; T_m = T_n \quad (25)$$

For heat sink inlets and outlets:

(a) At inlet: $V_f = V_{in}$ and T_{in} = 298K

(b) At outlet: gauge pressure P_{out} = 0

(c) No-slip condition at the solid-fluid interface.

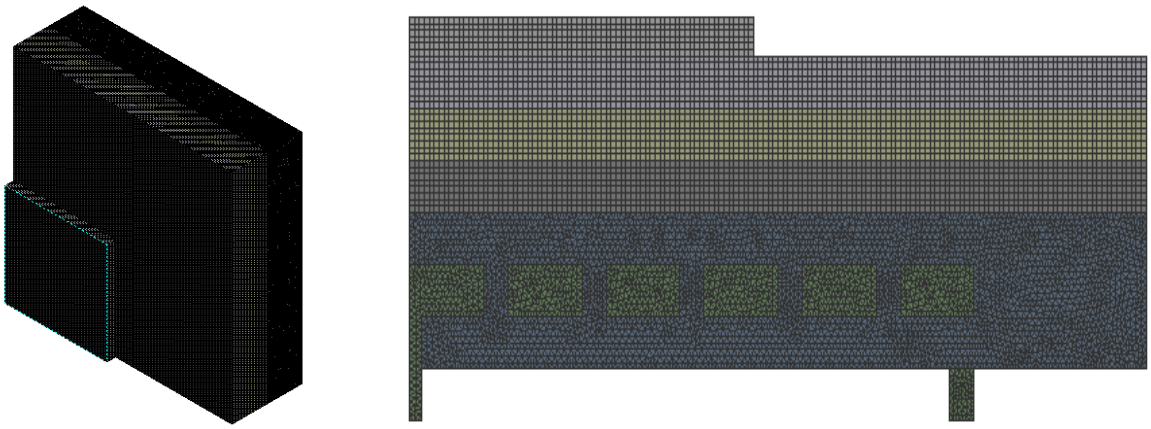
The side and bottom walls of the heat sink are given convective boundary conditions. The convective HTC is calculated using equation (22) and is estimated as 9.79 W/m^2·K.

In the present work, the governing equations using the boundary condition are solved by ANSYS Fluent 2020 R2. The discretization of continuity, momentum, and energy equations

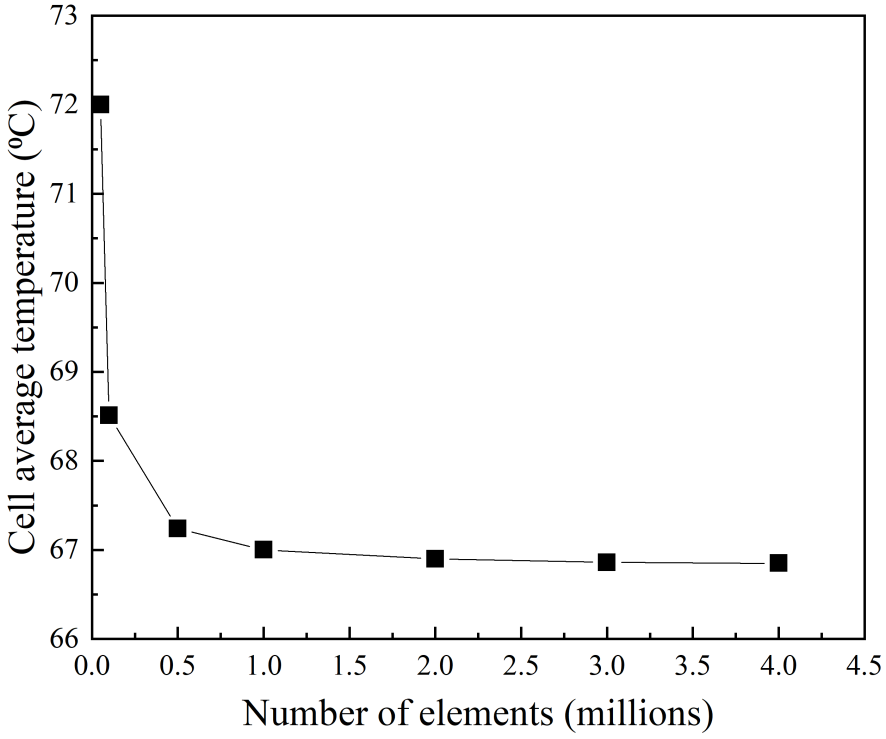
283 is performed by adopting the second-order upwind scheme using the SIMPLE algorithm. The
284 convergence criteria of 10^{-3}, 10^{-6} and 10^{-8} for the continuity, momentum and energy equations
285 are assigned. The source term in the energy equation is incorporated using a user-defined
286 function (UDF).

287 **3.4 Grid independence test**

288 The grid independence test is conducted for all channel configurations. The cell average
289 temperature is observed for different grid sizes at $\dot{m}$ = 25 g/min. Figure 3(a) shows the isometric
290 and front view of the meshed geometry. The number of elements chosen is 0.05, 0.1, 0.5, 1, 2,
291 3, and 4 million. Figure 3(b) shows the variation in cell average temperature with the number
292 of elements for channel configuration 5. The cell average temperature is observed to become
293 independent of the grid size after the number of elements became 2 million. The temperature
294 change is observed to be 0.05% after 2 million elements, which is quite negligible.



(a)



(b)

Figure 3. (a) Meshed geometry (b) Grid independence test for the channel configuration 5

4. Validation

The current numerical model is compared with the published results of Abo-Zahhad et al. [13]. The authors studied the effect of CJI on the performance of HCPV-T systems for different designs of heat sinks with various inlet configurations. Figure 4 shows the validation of the current numerical model with the results obtained by Abo-Zahhad et al. by comparing the cell average temperature for different mass flow rates at CR = 1000 suns and the ambient temperature of 25 °C. It is seen that the results of the current numerical model are in good agreement with those reported by Abo-Zahhad et al., with a maximum error of 1.8%.

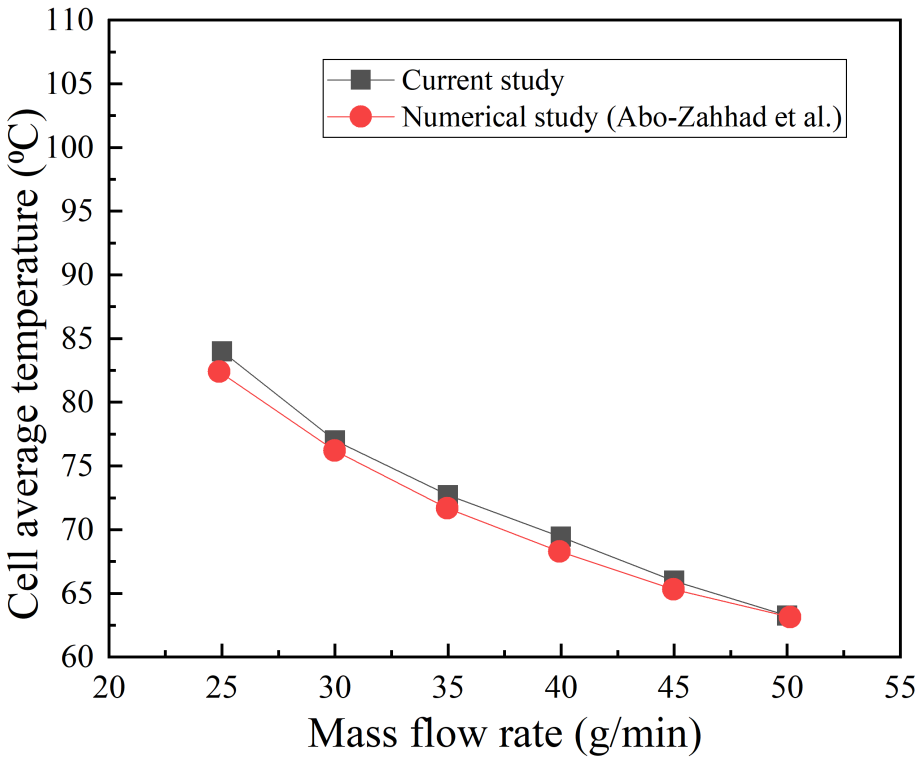


Figure 4. Validation of the current numerical model with literature

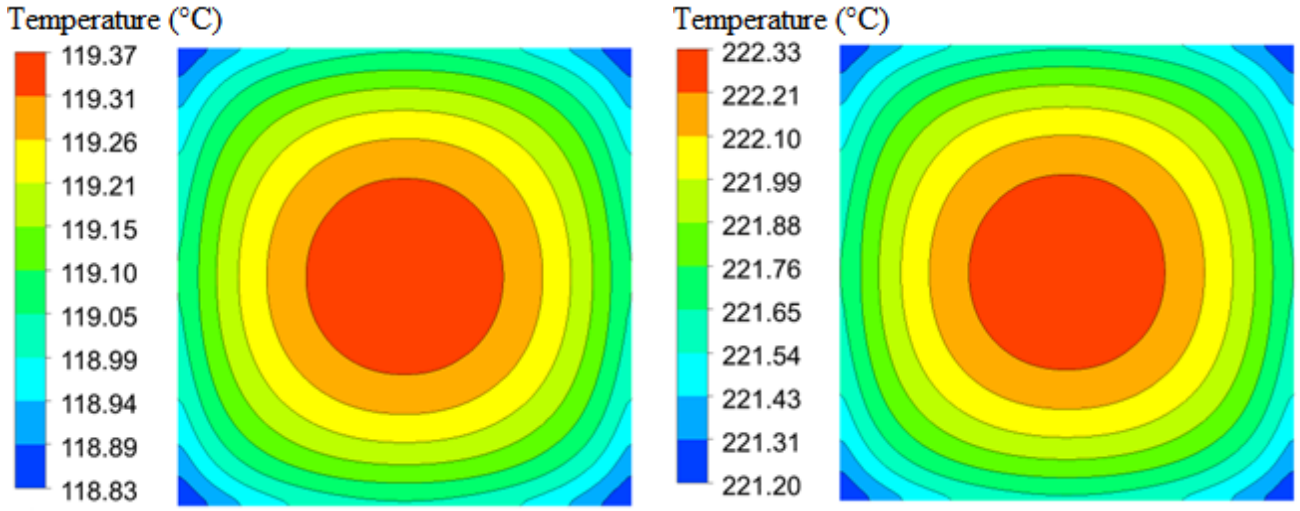
5. Results and Discussion

The present study investigates the influence of the CJI cooling scheme on the electrothermal performance of HCPV-T systems. A 25×25 mm aluminium heat sink is integrated at the backside of the solar PV cell and copper-ceramic assembly. Mixed convection and radiation boundary conditions are applied to the upper surface of the PV cell and copper layer, which are exposed to the environment. All sides of the solar cell, copper and ceramic assembly, and heat sink are subjected to convective boundary conditions.

5.1 Uncooled condition

The impact of high concentration on the CPV-T system's overall performance is evaluated for the uncooled condition. Figure 5 depicts the temperature contours over the cell top surface at various concentration ratios for uncooled conditions when the surrounding temperature is 25 °C. The maximum cell temperature reaches up to 876 °C at CR = 800, 686.7 °C at CR = 500, 222.3 °C at CR = 100, and 119.4 °C at CR = 50 under no cooling conditions.

The heat transfer in the solar PV cell is governed by conduction, and heat generation in the solar PV cell is a function of available solar radiation. This leads to the high temperature of the cell at higher concentration ratios. Therefore, the maximum temperature difference on the PV cell surface is 12.45 °C at *CR* = 800 under no cooling conditions. At low concentration levels, a more uniform distribution of temperature is observed over the cell surface. Since the heat generation increases at higher concentration ratios and the top surface and sides of the PV cell are given convective boundary conditions, the maximum temperature at the centre of the PV cell increases. At higher concentrations, this causes non-uniformity at the cell surface and an increase in temperature. The temperature non-uniformity over the surface of the PV cell is 0.54 °C at *CR* = 50, 1.13 °C at *CR* = 100, and 7.16 °C at *CR* = 500. A high non-uniformity of temperature over the cell surface leads to problems associated with current mismatching, leading to power losses. The high temperature of the solar PV cell leads to an increase in thermal stress over the cell surface. The maximum thermal stress is 145 MPa, 306 MPa, 1027 MPa, and 1323 MPa for *CR* = 50, 100, 500, and 800, respectively. The thermal stress for uncooled conditions is much higher than the yield limit of Germanium. It results in permanent deformation followed by fracture of the solar PV cell. Therefore, in order to achieve a consistent temperature at higher concentration ratios, the solar PV cells must be cooled.



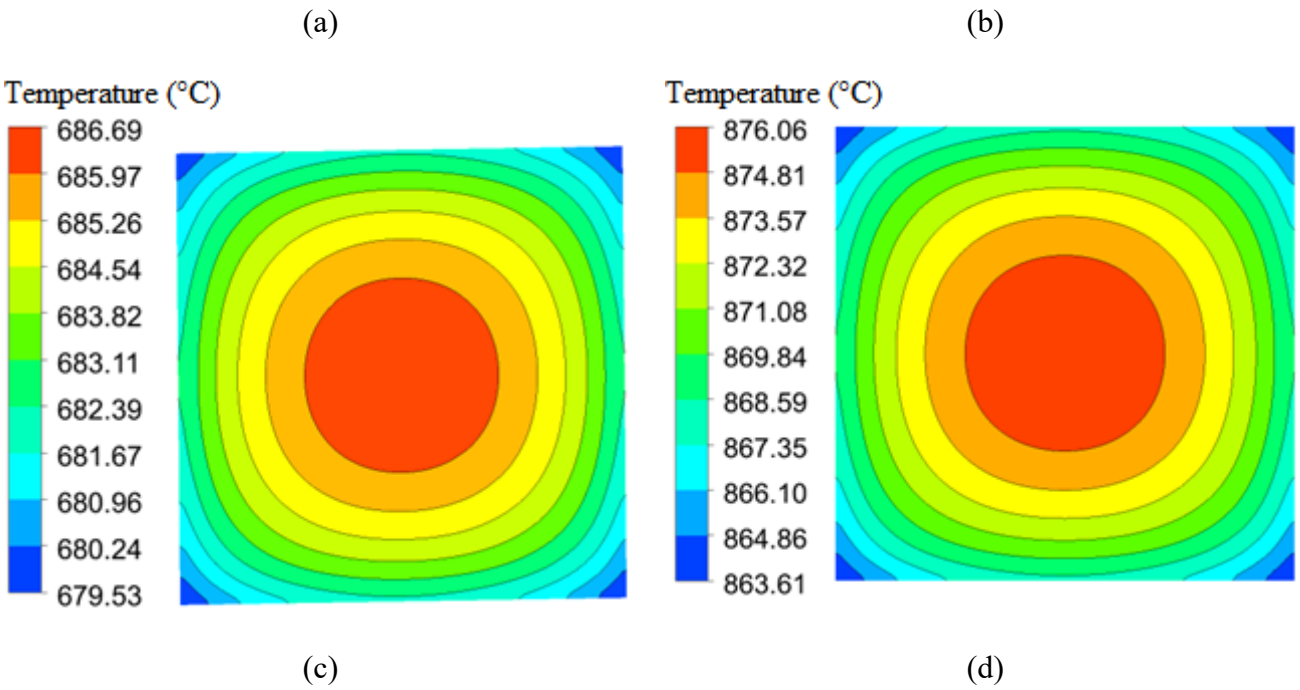
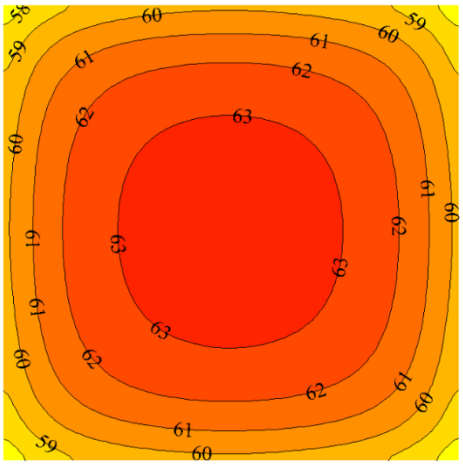


Figure 5. Temperature (°C) contour over cell top surface for uncooled conditions for (a) *CR* = 50, (b) *CR* = 100, (c) *CR* = 500 and (d) *CR* = 800

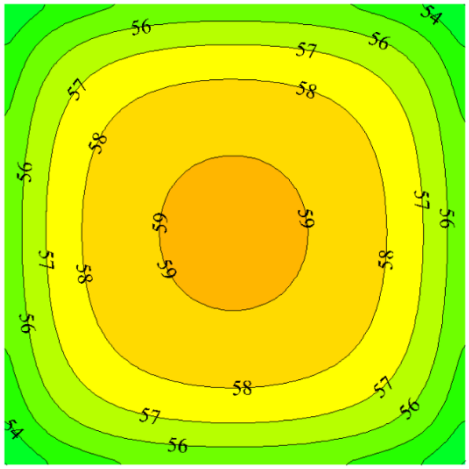
5.2 Cooled conditions

The CJI cooling technique is applied to HCPV-T systems to keep the temperature within the safe limit. The effect of the coolant mass flow rate on the electrical and thermal performance of the HCPV-T system is studied by varying the $\dot{m}$ to 25, 30, 35, 40, 45, and 50 g/min. The lower mass flow rate is set to 25 g/min to avoid the flow boiling phenomenon. The current study is limited to cooling of the HCPV-T system using single-phase flow. The maximum mass flow rate is set to 50 g/min to avoid a sharp increase in pressure drop across the heat sink, which will reduce the net power output generated by the solar cell. Channel configuration 1 is considered for this analysis for *CR* = 1000. At a concentration ratio of 1000, the temperature contour over the cell top surface of the rectangular channel cooling system is depicted in Figure 6. It has been noted that the maximum and average cell temperatures decrease when ṁ rises. The temperature on the cell top surface reduces from 63.55 °C for $\dot{m}$ = 25 g/min to 51 °C for $\dot{m}$ = 50 g/min. As the mass flow rate rises, the kinetic energy of the jet increases. Higher mass flow rates cause the jet to impinge more forcefully on the heat sink

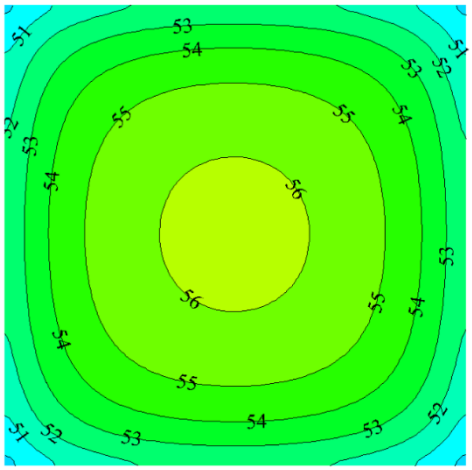
surface, increasing the convective heat transfer coefficient as more kinetic energy is transformed into pressure energy. As the coolant mass flow rate increases, the surface temperature decreases. Additionally, it has been noted that when $\dot{m}$ increases, the maximum temperature uniformity significantly falls. The quantity of thermal energy that the coolant extracts from the PV cell reduces as the $\dot{m}$ increases because the flow residence time is shortened. The temperature homogeneity on the PV cell surface decreases as a result.



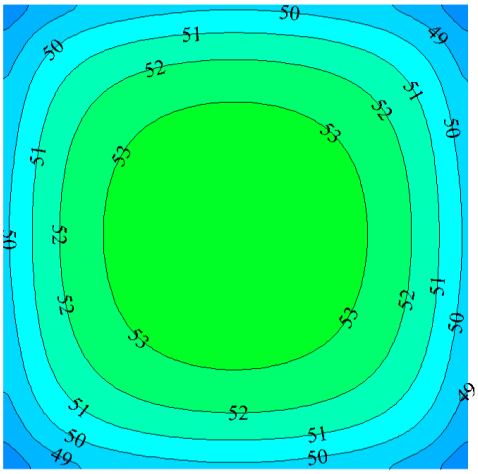
(a)



(b)



(c)



(d)

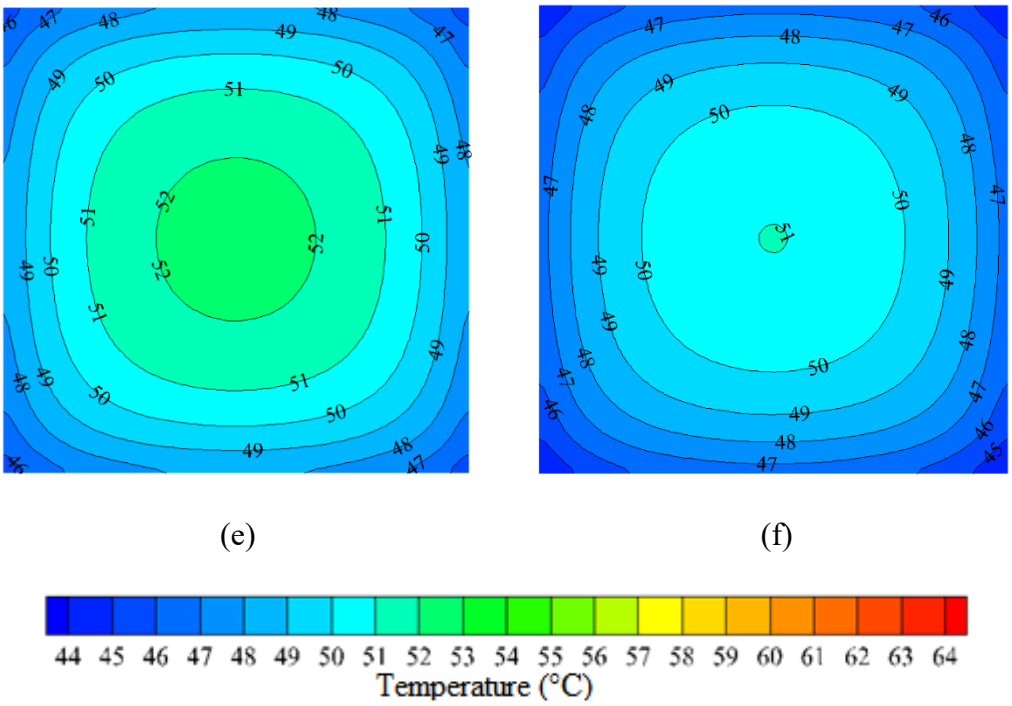
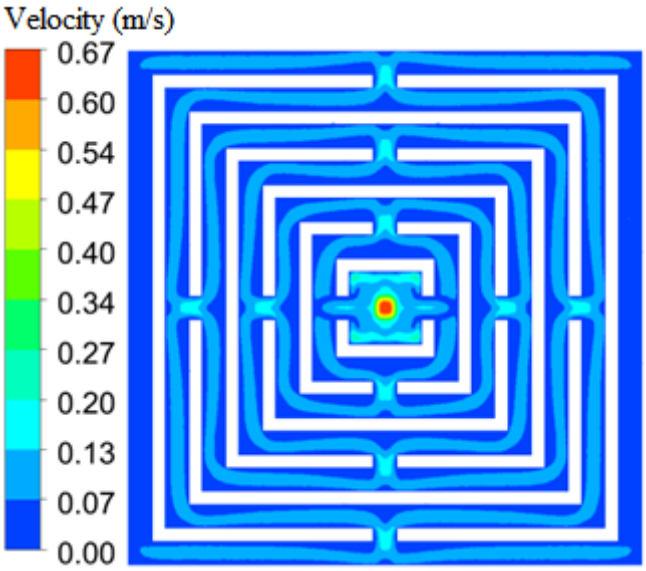


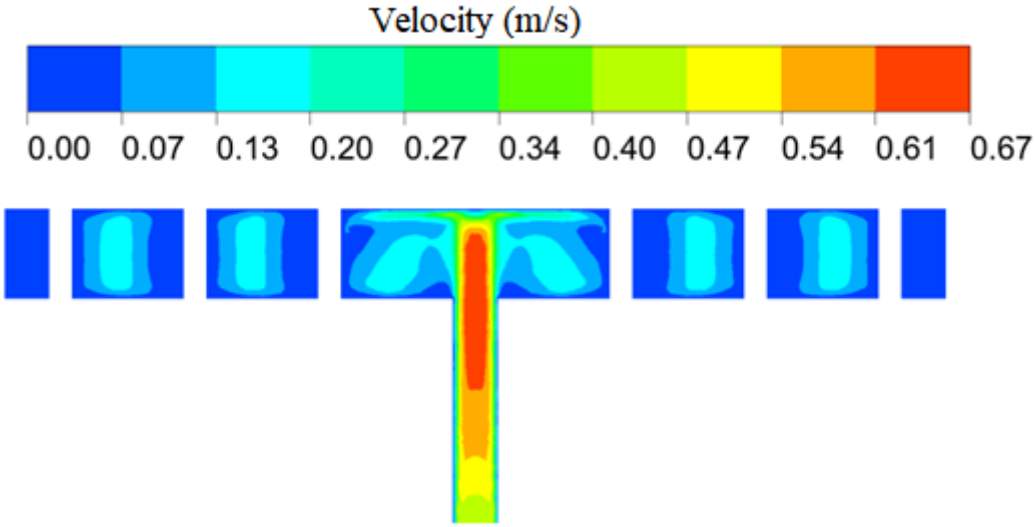
Figure 6. Temperature (°C) contour over cell top surface for configuration 1 for mass flow rates of (a) 25, (b) 30, (c) 35, (d) 40, (e) 45 and (f) 50 g/min

Figure 7(a) predicts the contour of velocity over the parallel mid-section plane of the fluid domain for configuration 1 at $\dot{m}$ = 25 g/min and CR = 1000. The coolant velocity is maximum at the centre of the structure, where the jet enters the channel. As the jet impinges on the heat sink surface, the kinetic energy of the cooling fluid converts into pressure energy. As the coolant flows along the length of the channel, the coolant splits into two parts, and the velocity reduces. The effect of the hydrodynamic boundary layer on the coolant velocity can also be observed from the figure. Near the boundary region, the velocity of the cooling fluid is zero due to no-slip boundary conditions on the surface and is maximum at the centre of the cross-section of the channel. Figure 7(b) illustrates the velocity contour over the perpendicular mid-section plane of the fluid domain for channel configuration 1 at the same conditions. At the entrance of the inlet, the velocity of the jet is equal to the free stream velocity. As the jet enters the inlet section, the hydrodynamic boundary layer grows in the developing region. The effect of viscosity can be observed in the contour. Hence, to compensate for the total mass flow

rate of the cooling fluid, the maximum velocity in the central region of the jet increases. As the jet flows further along the inlet tube, the velocity in the central region of the jet reaches its maximum and strikes the heat sink surface.



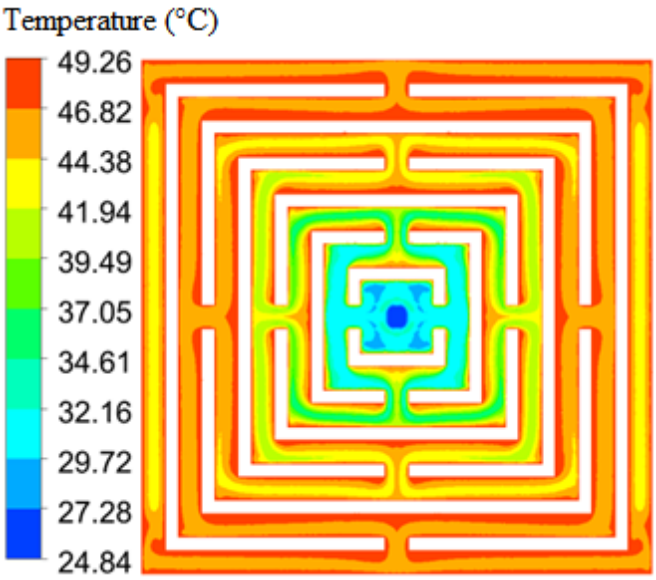
(a)



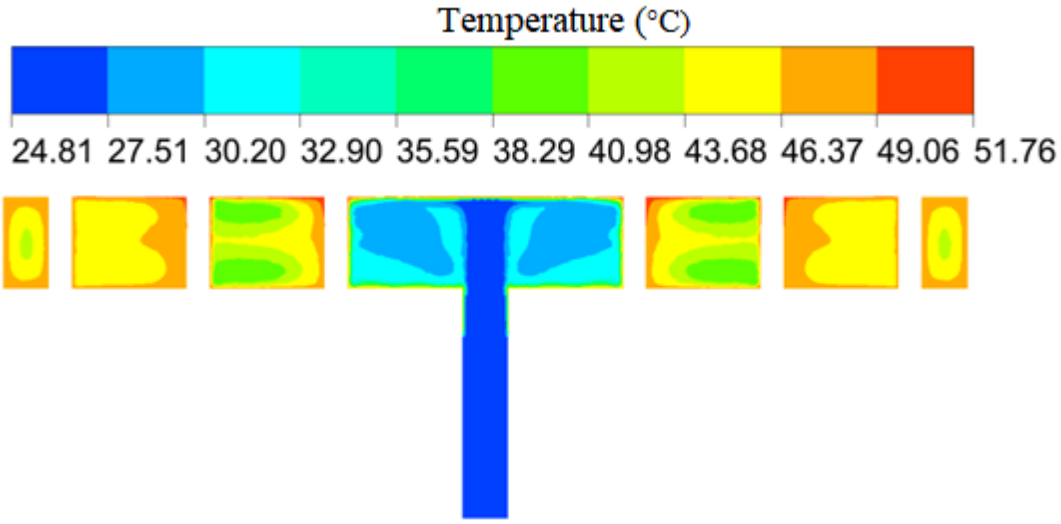
(b)

Figure 7. Velocity (m/s) contour on (a) parallel mid-section plane and (b) perpendicular mid-section plane of the fluid domain for configuration 1 at $\dot{m}$ = 25 g/min

Figures 8(a) and 8(b) show the temperature contour over the parallel and perpendicular mid-section plane, respectively, of the fluid domain for configuration 1 at $\dot{m}$ = 25 g/min and CR = 1000. It can be observed that the temperature of the coolant is minimal at the centre of the heat sink due to the stagnation effect. The coolant temperature increases as it flows along the length of the channel due to the thermal energy being removed from the PV cell. The temperature of the coolant increases from 25 °C at the inlet to 49 °C at the outlet. The thermal boundary layer thickness is higher near the top surface than the bottom surface of the channel, as heat is conducted from the PV cell to the top wall of the channel.



(a)



(b)

Figure 8. Temperature (°C) contour on the (a) parallel mid-section plane and (b) perpendicular mid-section plane of the fluid domain for configuration 1 at $\dot{m}$ = 25 g/min

Figure 9 shows the variation in convective heat transfer coefficient along the length of the channel. It is observed that the value of h is at its maximum at the centre of the channel. As the jet strikes the heat sink surface at the centre, there is a stagnation point, and the HTC at the stagnation point is the highest. The thermal boundary layer starts to form from the stagnation point. Hence, the temperature gradient in the direction of heat transfer is at its maximum at the stagnation point. This leads to an enhanced surface heat coefficient at the stagnation point. As the coolant flows along the length of the channel, the HTC reduces because of the formation of the hydrothermal boundary layer. This helps in achieving a more homogeneous temperature distribution over the cell surface.

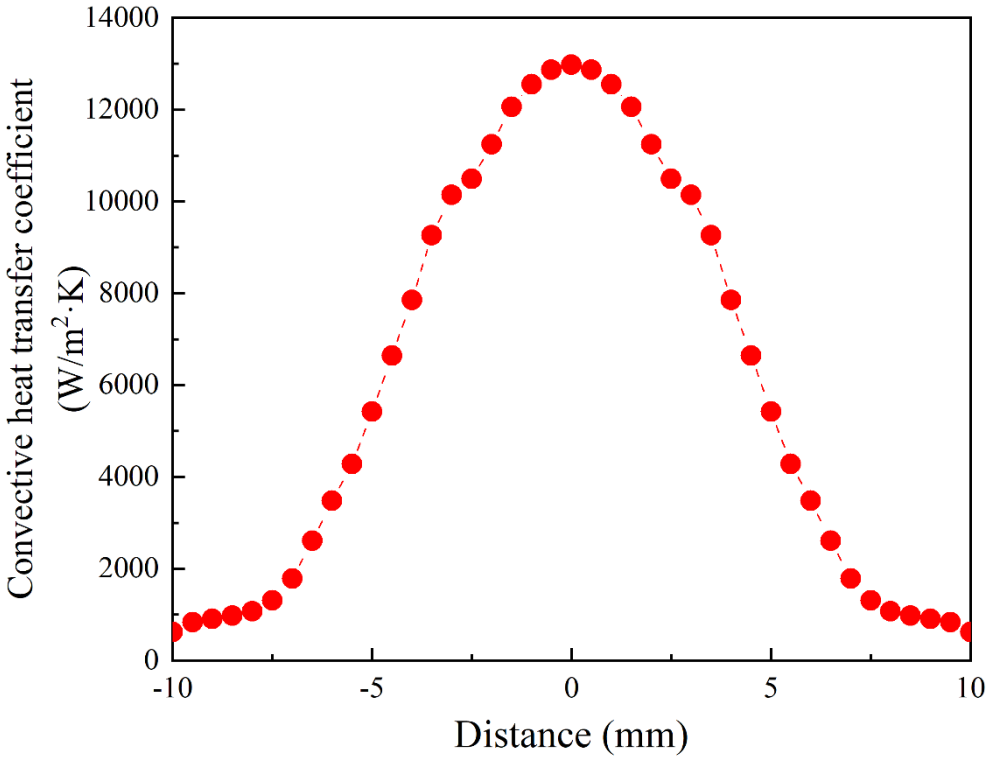
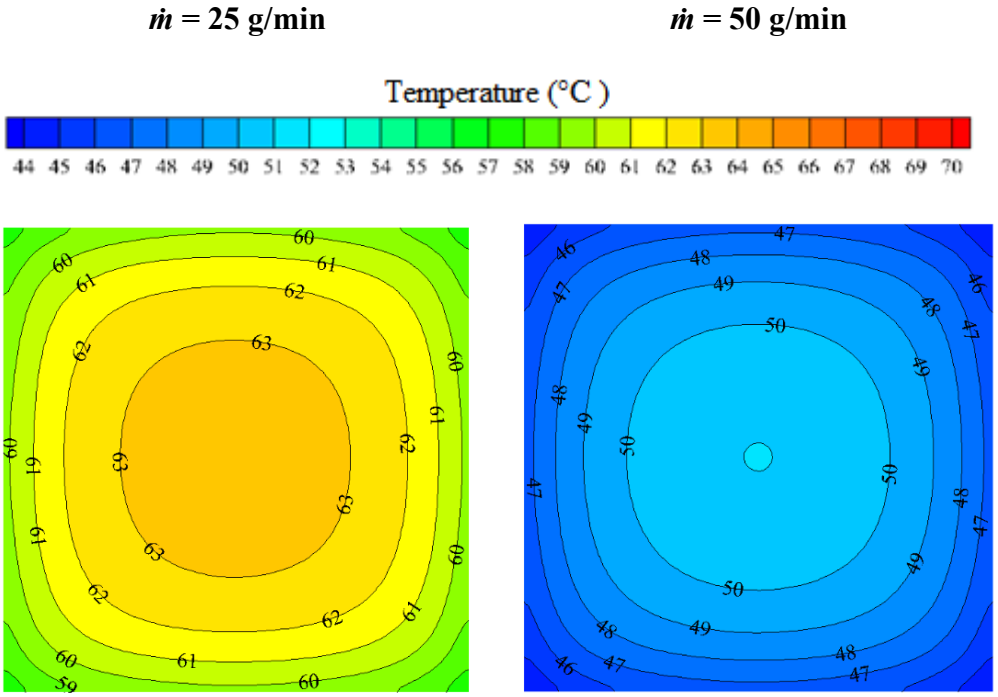


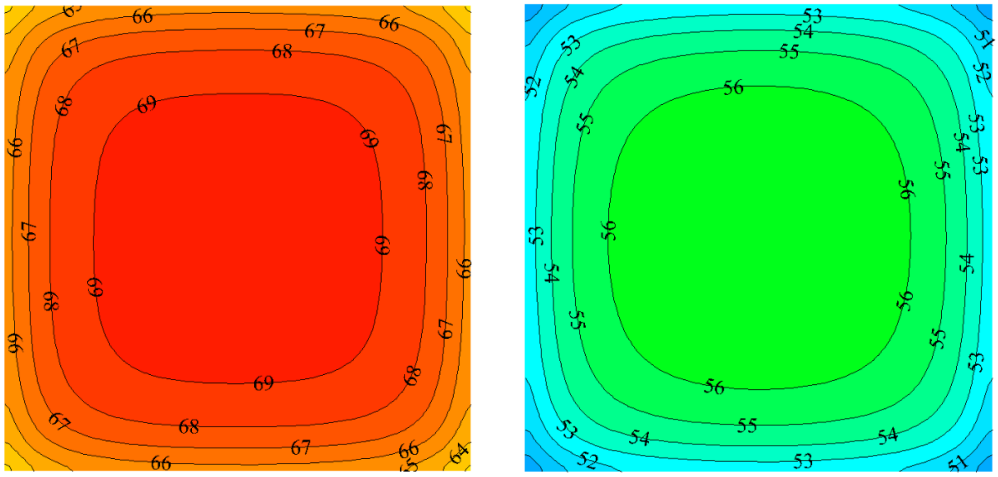
Figure 9. Variation in convective HTC along the channel length

5.3 Effect of channel geometry

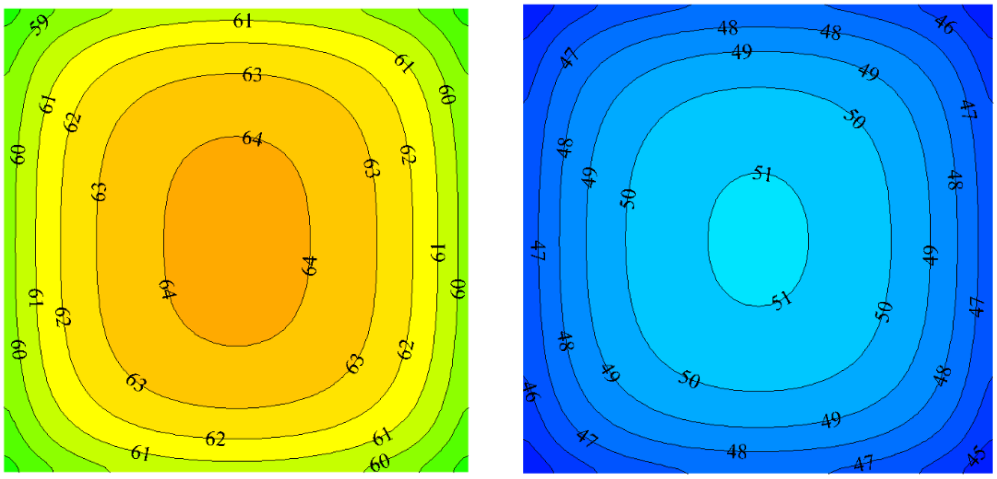
The effects of channel geometry and mass flow rate of coolant on the electrical and thermal performance of the HCPV-T system are investigated by considering five configurations, as shown in Figure 2, for two flow rates of 25 and 50 g/min. Figure 10 depicts the temperature contours over the cell top surface for all the channel configurations for two different values of $\dot{m}$. The maximum temperature of the PV cell reduces from 975.9 °C in uncooled conditions to 63.4 °C, 69.3 °C, 64.3 °C, 68.07 °C, 69.1 °C for configurations 1, 2, 3, 4, 5 respectively, with $\dot{m}$ = 25 g/min at CR = 1000. The minimum cell temperature is obtained for channel configuration 1. Since the distribution of the coolant is uniform with channel configurations 1 and 3, it results in a reduction in the average temperature of the solar PV cell. Since the HTC increases with increasing coolant mass flow rate, it considerably reduces cell average temperature.



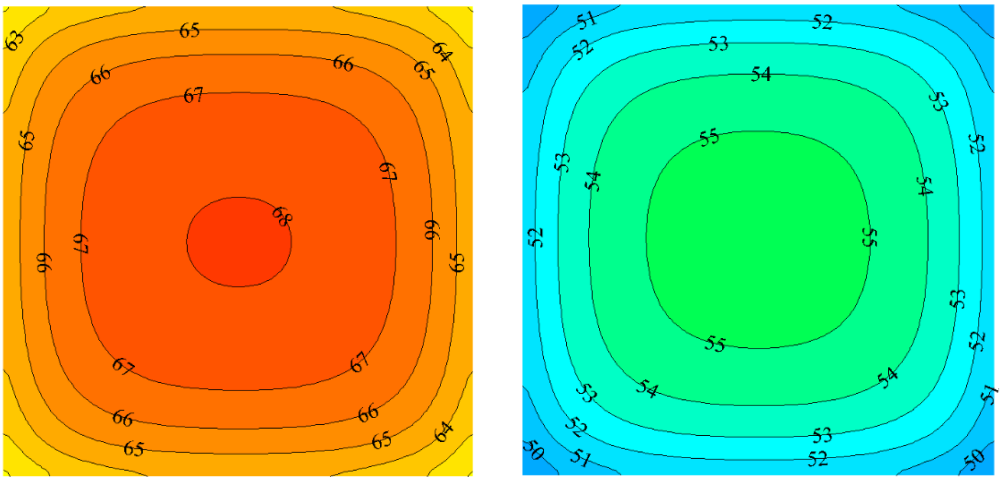
(a)



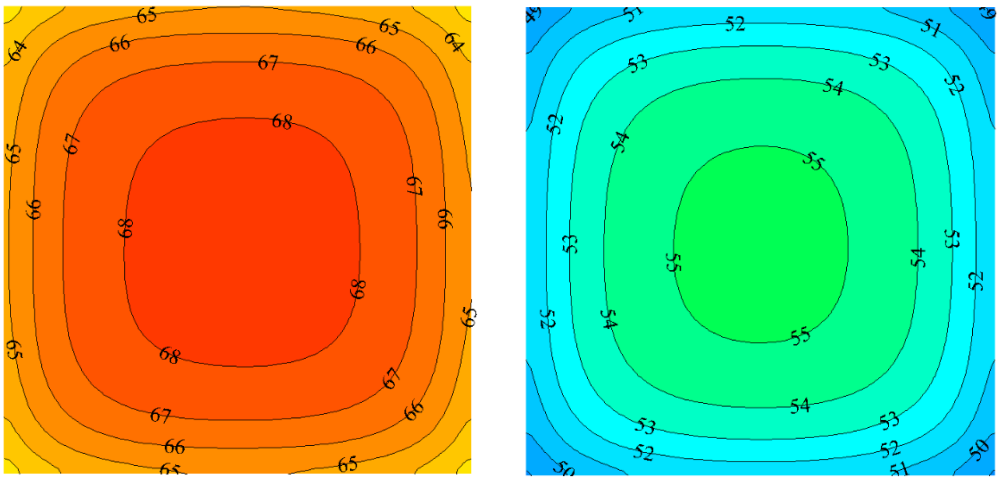
(b)



(c)



(d)

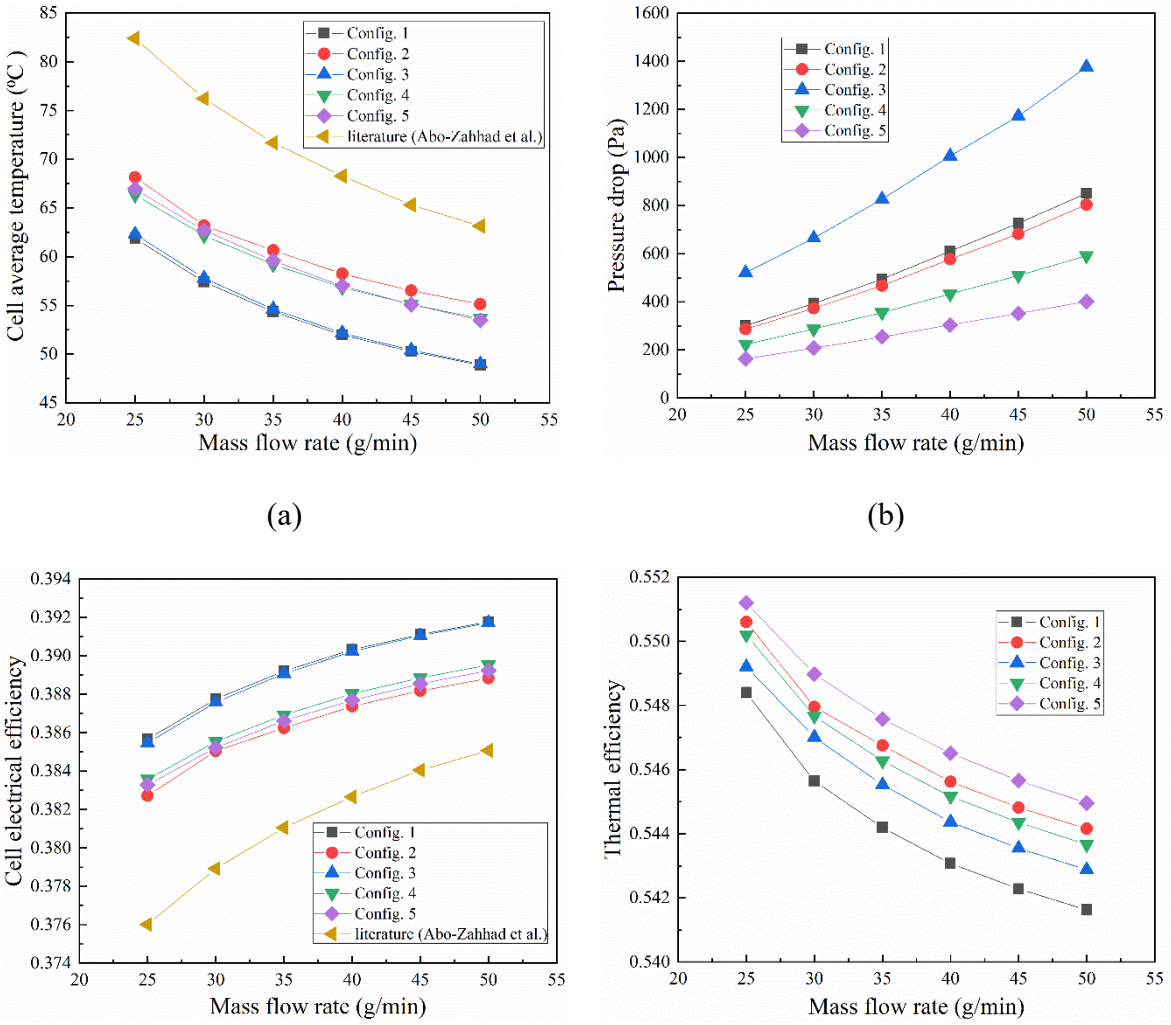


(e)

Figure 10. Temperature contour over cell top surface at CR = 1000 for (a) channel configuration 1, (b) channel configuration 2, (c) channel configuration 3, (d) channel configuration 4, and (e) channel configuration 5

5.4 Effect of coolant mass flow rate

Figure 11(a) displays the variation in cell average temperature with varying $\dot{m}$ for all the channel configurations. The cell average temperature is 61.8 °C, 68.1 °C, 62.3 °C, 66.3 °C, 66.9 °C at $\dot{m}$ = 25 g/min, which decreases to 48.9 °C, 55.1 °C, 49 °C, 53.6 °C, 53.4 at $\dot{m}$ = 50 g/min for channel configurations 1, 2, 3, 4, 5, respectively. The cell average temperature is minimal with channel configurations 1 and 3 and highest with channel configuration 2. Since the effective length of contact between the coolant and heat sink is shorter with channel configuration 2, it results in an increased average temperature of the cell. The average temperature of the cell using the present cooling method is lower by 16.6 °C than that reported by Abo-Zahhad et al. [13] under the same conditions. Furthermore, the cell average temperature reduces at higher coolant mass flow rates due to enhanced surface HTC.



435 Figure 11. Variations in (a) cell average temperature, (b) pressure drop, (c) cell electrical
436 efficiency and (d) thermal efficiency with $\dot{m}$

437 Figure 11(b) shows the pressure drop variation with $\dot{m}$ for all configurations. The
438 pressure drop is 301 Pa, 286 Pa, 521 Pa, 223 Pa, and 163 Pa for channel configurations 1, 2, 3,
439 4, and 5, respectively, at $\dot{m}$ = 25 g/min. The maximum pressure drop occurs with channel
440 configuration 3. This happens due to 180° bends at each corner. The adverse pressure gradients
441 near the outer and inner walls of the bends lead to increased pressure losses. It has been
442 observed that the pressure losses are minimal with channel configuration 5. The flow is split
443 into parts at each junction and mixed at the outlet. Hence, the pressure drop is minimal for
444 channel configuration 5. It is found that the pressure drop across the heat sink is significantly

lower than that reported by Tang et al. [14] because of the mini-scale channel configurations in the present heat sink. The pressure drop across the heat sink increases for the increasing mass flow rate, since it is proportional to the flow rate of the coolant.

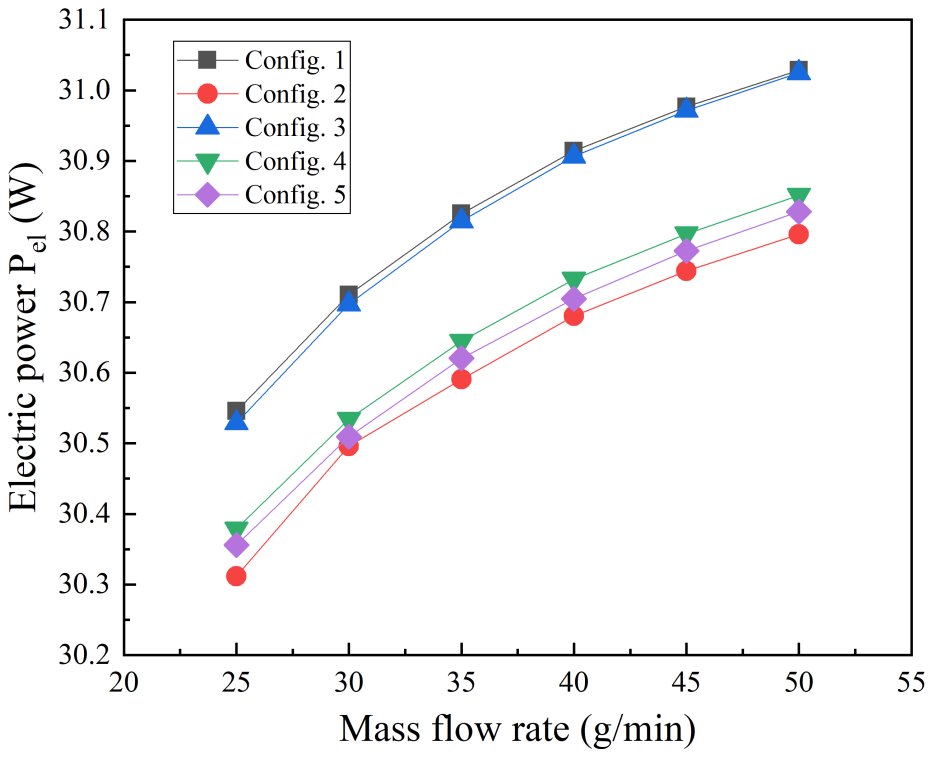
Figure 11(c) shows the variation in cell electrical efficiency (η_{cell}) with $\dot{m}$ for all channel configurations. The cell electrical efficiency is 38.5%, 38.2%, 38.5%, 38.3%, and 38.3% for channel configurations 1, 2, 3, 4, and 5, respectively, for $\dot{m}$ = 25 g/min. The electrical efficiency of the PV cell depends on its operating temperature, according to equation 4. As the average cell temperature rises, the open circuit voltage of the cell reduces, resulting in a decrease in η_{cell}. Hence, η_{cell} is at its maximum with channel configurations 1 and 3 and is at its lowest with channel configuration 2.

Figure 11(d) exhibits the variation in thermal efficiency with coolant flow rates for all channel configurations. The cell thermal efficiency is at its maximum of 55.1% with channel configuration 5 and is at its minimum of 54.8% with channel configuration 1. The cooling fluid temperature at the outlet is maximum with channel configuration 5 as the thermal energy extracted by the coolant is higher with channel configuration 5. This results in a higher η_{th} of the system with channel configuration 5. It is also observed that with an increased $\dot{m}$, there is a decrease in η_{th} of the PV cell due to a decrease in the available energy transformed into useful heat. As the electrical efficiency of the PV cell increases, the thermal efficiency decreases.

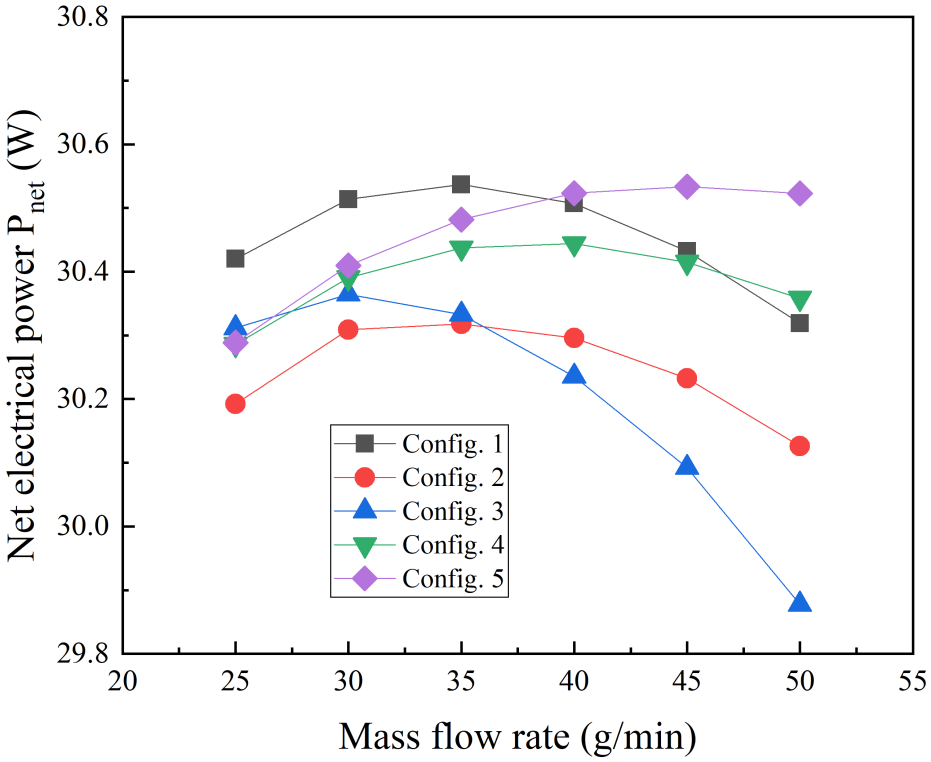
A. Electrical power

Figure 12(a) shows the variation in the generated electric power (P_{el}) for different $\dot{m}$ for all channel configurations. It can be noted that the efficiency of the considered cell insignificantly changes throughout the day, as depicted in the datasheet [16]. The change in the solar irradiation from ×250 to ×1000 results in a slight variation in the cell efficiency value due to increased thermal losses within the cell; however, the produced power changes considerably. In this study, cell electrical efficiency is evaluated for different coolant mass flow rates at a

given solar irradiation, and the generated electrical power is directly proportional to the cell electrical efficiency for particular solar irradiation and CR. Hence, the P_{el} is maximum with channel configurations 1 and 3 and is minimal with channel configuration 2. Figure 12(b) depicts the variation in net electrical power generated by the CPVT system with $\dot{m}$ for all channel configurations. At higher mass flow rates, the net electrical power is at its maximum for channel configuration 5. Since the pressure drop is minimal with channel configuration 5, the net electrical power is maximum at higher coolant mass flow rates for this case. Although P_{el} is at its maximum with channel configuration 1, the pressure losses increase with an increase in flow rate with channel configuration 1. This results in a reduction in net generated electrical power with channel configuration 1. Hence, channel configuration 5 is the best at higher coolant mass flow rates, producing the maximum net electrical power.



(a)



(b)

Figure 12. Variation in (a) cell electric power and (b) net electric power with $\dot{m}$

B. Temperature non-uniformity

Figure 13 shows the variation in temperature non-uniformity with $\dot{m}$ for all channel configurations. The temperature non-uniformity is minimal with channel configuration 5 and is equal to 5.7 °C at $\dot{m}$ = 25 g/min. The effective length of contact between coolant fluid and heat sink is less with channel configuration 2. Hence, the temperature non-uniformity is at its maximum with channel configuration 2. The temperature non-uniformity at $\dot{m}$ = 50 g/min is 6.8 °C, 7.6 °C, 7 °C, 6.3 °C, and 6.3 °C, respectively, for configurations 1, 2, 3, 4, and 5. As $\dot{m}$ increases, the thermal energy removed by the coolant from the heat sink reduces due to a lesser residence time of the coolant in the channel. This results in a rise in temperature non-uniformity over solar PV cell surface. The temperature uniformity over the cell surface is higher in this study than that reported by Dong et al. [11] and Shohdy et al. [15], as mentioned earlier, due to the incorporation of the channel configurations in the heat sink. The variation in HTC along the channel length helps maintain a more homogeneous temperature over the solar PV cell

surface. At the centre of the PV cell, the maximum cell temperature occurs; therefore, the jet is designed to impinge at the centre of the cell to have maximum convective heat transfer.

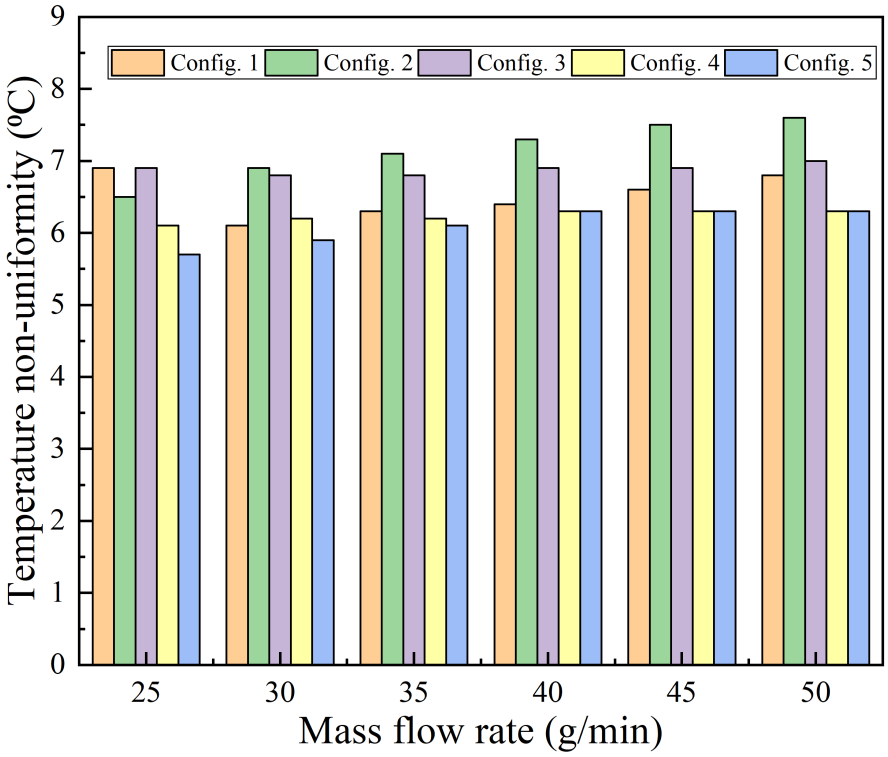
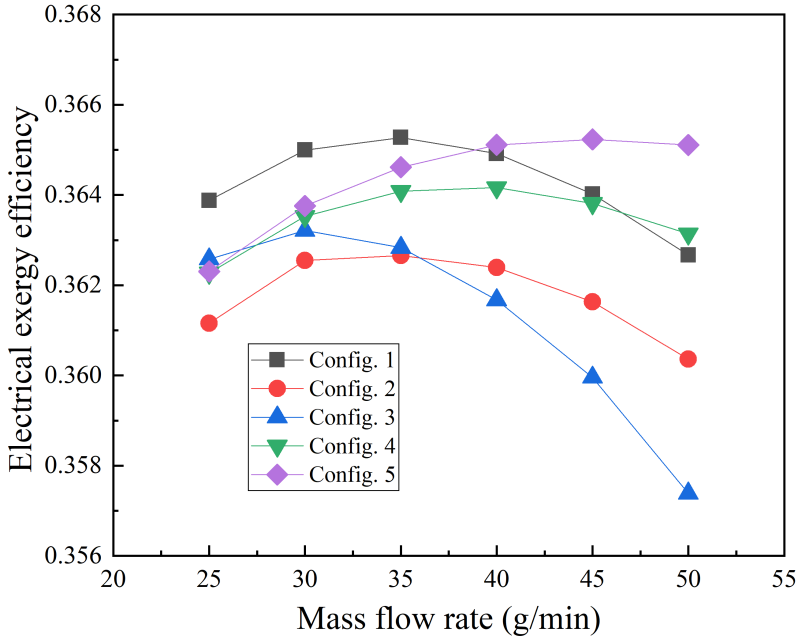


Figure 13. Variation in temperature non-uniformity with coolant mass flow rate

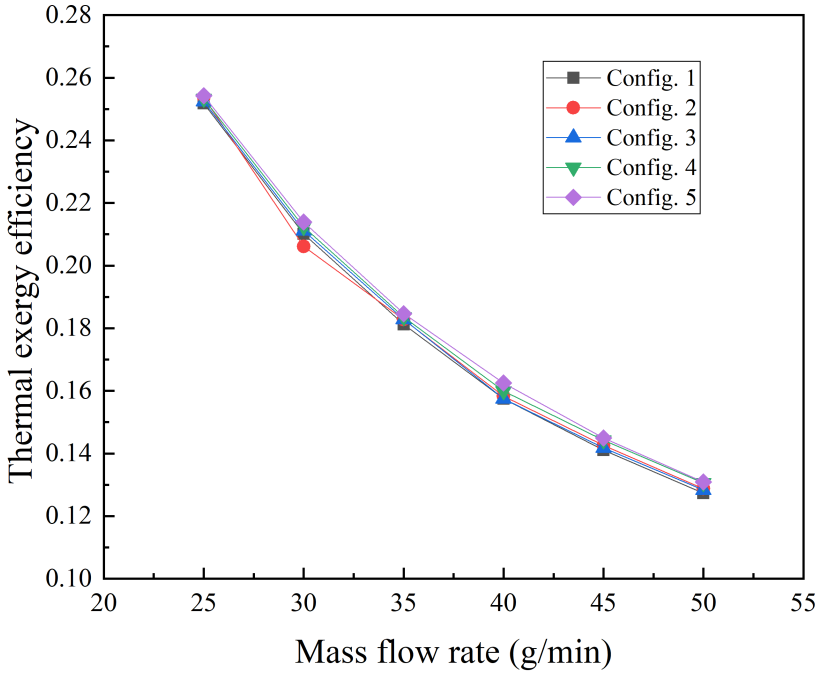
C. Cell exergy efficiency

Figure 14(a) shows variation in electrical exergy efficiency with coolant flow rates for all channel configurations. The electrical energy can be fully converted to heat energy. Hence, the net electrical power, accounting for the difference between the electrical energy produced and the frictional power loss, is considered to be electrical exergy. Hence, it follows the same trend as the net electrical power generated. At higher values of $\dot{m}$, the maximum electrical exergy of 0.365 at $\dot{m}$ = 50 g/min is obtained with channel configuration 5 and is minimal of 0.357 at $\dot{m}$ = 50 g/min with channel configuration 3. Figure 14(b) depicts the variation in thermal exergy efficiency with $\dot{m}$. Out of the total thermal energy, the maximum amount of work that can be obtained depends on the temperature at which thermal energy is obtained. Thermal energy is not entirely available for the production of useful work. The trend of

variation in thermal exergy with mass flow rate is similar to the variation in thermal energy. The maximum thermal exergy of 0.25 is obtained at $\dot{m}$ = 25 g/min with channel configuration 5. It signifies that out of 55.1% of thermal efficiency, only 25% of the energy can be converted into useful work for channel configuration 5 at $\dot{m}$ = 25 g/min.



(a)



(b)

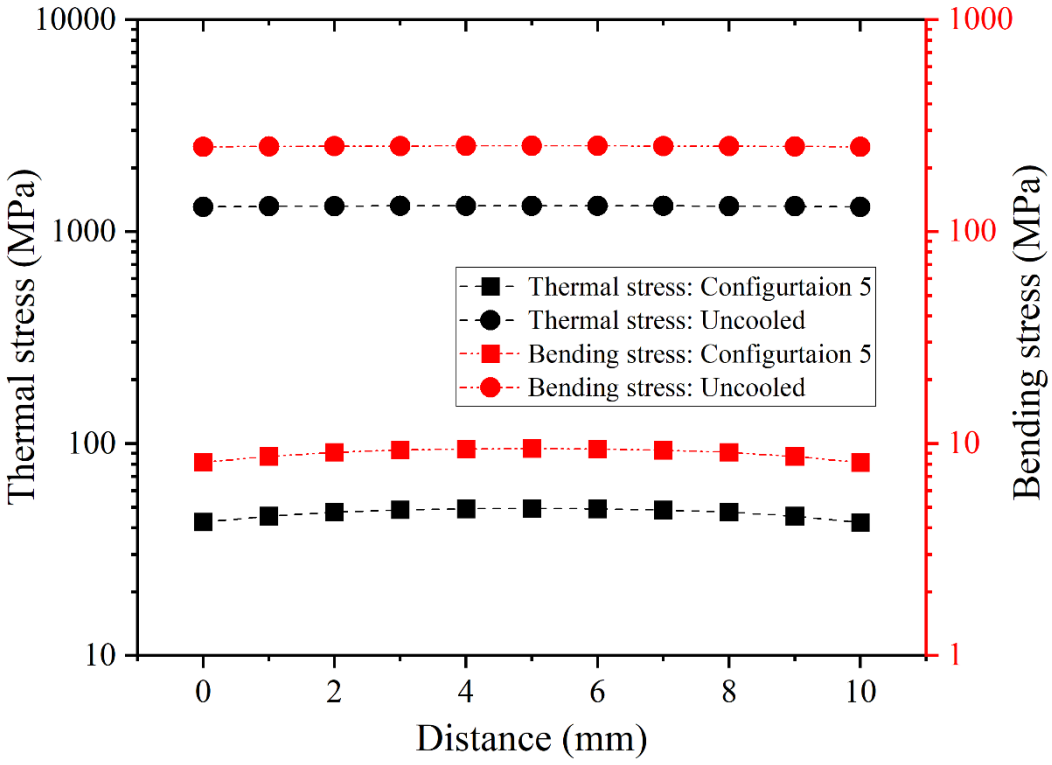
Figure 14. Variation in (a) electrical exergy and (b) thermal exergy efficiencies with $\dot{m}$

524 **D. Thermal and bending stresses**

525 Figure 15 shows the local thermal and bending stress distributions on PV cells for
526 configuration 5 and uncooled conditions reaching cell temperature at 876 °C. It has already
527 been observed that temperature gradients exist over the solar PV cell surface. Since the
528 Germanium layer is attached to the copper layer, this leads to thermal stress generation on the
529 solar PV cell surface. The thermal stress is maximum at the centre of the PV cell surface, as
530 the maximum temperature difference occurs at the centre of the PV cell. As the distance
531 increases gradually along the centre line from the centre, the thermal stress decreases because
532 of the lower temperature difference over the solar PV cell surface. The maximum thermal stress
533 is 49.4 MPa at the centre, and the minimum thermal stress is 42.6 MPa at the edges for
534 configuration 5. In uncooled conditions, the maximum and minimum thermal stresses are 1323
535 MPa and 1307.55 MPa, respectively. The yield limit of the Germanium layer is 135 MPa. The
536 thermal stress for uncooled conditions is much higher than the yield limit of the Germanium
537 cell. Hence, it results in a plastic deformation followed by a fracture of the PV cell.

538 The bending stress distribution in the PV cell for configuration 5 at $\dot{m}$ = 50 g/min can
539 be observed. There is no slip between the Germanium and copper layers. This results in tensile
540 stress in the germanium PV cell layer and compressive stress in the copper layer due to
541 disparate values of CTE. The total strain in the Germanium layer is the summation of strain
542 due to temperature change and the strain due to bending stress. The maximum bending stress
543 occurs at the centre of the PV cell due to the high temperature at the centre. The maximum
544 bending stress is 9.47 MPa at the centre, and the minimum bending stress is 8.13 MPa at the
545 edges. The maximum deflection of 12 μm occurs at the centre of the PV cell. The bending
546 stress is well within the yield limit of the Germanium layer. Hence, the generated bending stress
547 is not significant. However, the bending stress is 238 MPa with a maximum deflection of 300
548 μm at the centre of the PV cell for the uncooled conditions where the cell temperature reaches

549 up to 876 °C. In uncooled conditions, it results in the bending of the PV cell beyond the elastic
550 limit and causes permanent deformation of the PV cell, affecting its working life. Therefore,
551 the cooling of PV cells is essential to restrict the thermal and bending stresses within an elastic
552 limit.



553

554 Figure 15. Thermal and bending stresses in the PV cell of configuration 5 for $\dot{m}$ = 50 g/min

555 **5.5 Effect of channel gap**

556 Figure 16 shows the effect of the gap between channels on the CPV-T system
557 performance. The cell average temperature is 53.45 °C, 53.9 °C, and 54.4 °C with the channel
558 gap 0.5 mm, 0.8 mm, and 1 mm, respectively. The cell average temperature increases with an
559 increase in the gap between channels. Since the number of passes for the coolant to flow in
560 channels reduces with an increase in channel gap, this increases the cell average temperature.
561 This also increases temperature non-uniformity over the cell surface because the contact path
562 length between the coolant and the heat sink reduces.

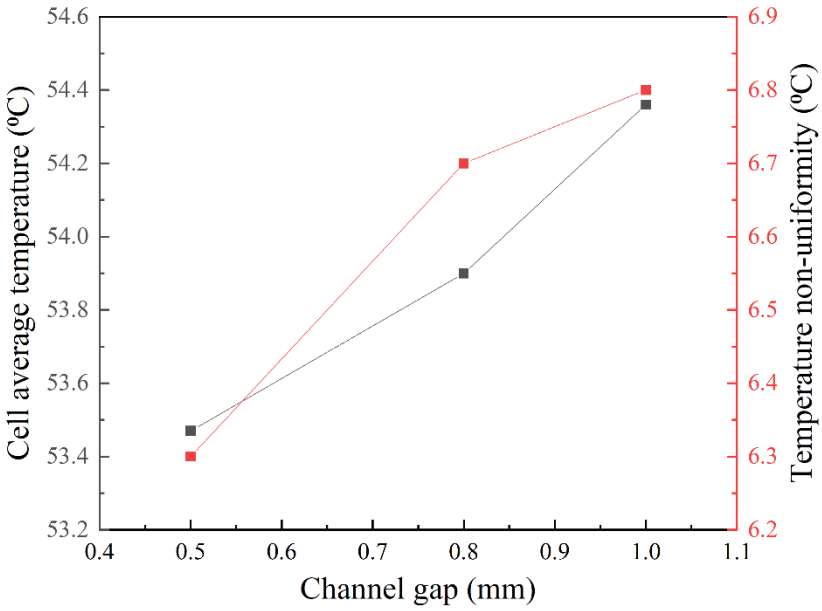


Figure 16. Effect of channel gap on cell average temperature and temperature non-uniformity

6. Conclusions

This paper evaluates the effectiveness of the confined jet impingement (CJI) cooling technique on the performance of highly concentrated photovoltaic thermal systems. Five different channel designs are proposed in this study. The performance of the HCPV-T systems is observed at different inlet mass flow rates for each of the channel configurations. All the channel configurations achieve the cell average temperature within permissible limits of 110 °C. Channel configuration 1 reaches the minimum cell average temperature. However, the net electrical power is reduced for higher mass flow rates with channel configuration 1 since the pressure drop increases sharply at higher mass flow rates. The pressure drop is minimal with channel configuration 5, which is a quadrant mini-channel with a single inlet. At higher mass flow rates, the net electrical power reaches a maximum with channel configuration 5. The temperature of the coolant at the outlet is the maximum for channel configuration 5, and the thermal efficiency is maximum with channel configuration 5. The highest temperature uniformity is obtained with the channel configuration 5. Hence, the thermal stress over the PV

cell surface is minimal with the channel configuration 5. Hence, the optimum channel configuration is configuration 5. The maximum and minimum thermal and bending stresses occur at the centre and edge of the cell, respectively; however, the lowest stress values are found for channel configuration 5. The bending stress of the centre of the PV cell is significantly lower with channel configuration 5 compared to the uncooled conditions. The proposed channel will be useful in cooling the highly concentrated PV-T system and achieving high electrical and thermal efficiencies with better temperature uniformity, thereby eliminating the problems associated with current mismatching and hotspots. The mini-channel configurations eliminate the problems associated with flow maldistribution and high-pressure drops. Moreover, the proposed channel configurations can be employed in the study of hybrid cooling systems such as CJI and thermoelectric cooling of CPV-T systems. The channels have been designed in such a way that the maximum cooling occurs at the highest temperature zone and then decreases along the path to achieve uniform surface temperature.

Data Availability

Data is available on request from the authors.

Acknowledgements

We express our gratitude to the Department of Science and Technology, India (DST) for providing financial support (TAR/2020/000358) for this study.

References

[1] World energy assessment. United Nations Development Programme; 2000.

[2] International energy outlook 2016 with projections to 2040. U.S. Energy Information Administration; 2016

[3] Dwivedi P, Sudhakar K, Soni A, Solomin E, Kirpichnikova I. Advanced cooling techniques of P.V. modules: A state of art. Case Stud Therm Eng 2020;21:100674. https://doi.org/10.1016/j.csite.2020.100674.

[4] Theristis M, O'Donovan TS. Electrical-thermal analysis of III-V triple-junction solar cells under variable spectra and ambient temperatures. Sol Energy 2015;118:533–46. https://doi.org/10.1016/j.solener.2015.06.003.

[5] Royne A, Dey CJ. Design of a jet impingement cooling device for densely packed PV cells under high concentration. Sol Energy 2007;81:1014–24. https://doi.org/10.1016/j.solener.2006.11.015.

[6] Javidan M, Moghadam AJ. Experimental investigation on thermal management of a photovoltaic module using water-jet impingement cooling. Energy Convers Manag 2021;228. https://doi.org/10.1016/j.enconman.2020.113686.

[7] Bahaidarah HMS. Experimental performance evaluation and modeling of jet impingement cooling for thermal management of photovoltaics. Sol Energy 2016;135:605–17. https://doi.org/10.1016/j.solener.2016.06.015.

[8] Zubeer SA, Ali OM. Experimental and numerical study of low concentration and water-cooling effect on PV module performance. Case Stud Therm Eng 2022;34:102007. https://doi.org/10.1016/j.csite.2022.102007.

[9] Markal B, Varol R. The Effect of Jet Impingement on the Performance of a Photovoltaic Module 2019;4:647–50.

[10] Amanlou Y, Tavakoli Hashjin T, Ghobadian B, Najafi G. Air cooling low concentrated photovoltaic/thermal (LCPV/T) solar collector to approach uniform temperature distribution on the PV plate. Appl Therm Eng 2018;141:413–21. https://doi.org/10.1016/j.applthermaleng.2018.05.070.

[11] Dong J, Zhuang X, Xu X, Miao Z, Xu B. Numerical analysis of a multi-channel active

cooling system for densely packed concentrating photovoltaic cells. Energy Convers Manag 2018;161:172–81. https://doi.org/10.1016/j.enconman.2018.01.081.

[12] Barrau J, Rosell J, Chemisana D, Tadrist L, Ibañez M. Effect of a hybrid jet impingement/micro-channel cooling device on the performance of densely packed PV cells under high concentration. Sol Energy 2011;85:2655–65. https://doi.org/10.1016/j.solener.2011.08.004.

[13] Abo-Zahhad EM, Ookawara S, Radwan A, El-Shazly AH, ElKady MF. Thermal and structure analyses of high concentrator solar cell under confined jet impingement cooling. Energy Convers Manag 2018;176:39–54. https://doi.org/10.1016/j.enconman.2018.09.005.

[14] Tang J, Li X, Hu R, Mo Z, Du M. A novel designed manifold ultrathin micro pin-fin channel for thermal management of high-concentrator photovoltaic system. Int J Heat Mass Transf 2022;183. https://doi.org/10.1016/j.ijheatmasstransfer.2021.122094.

[15] Shohdy A, Emam M, Sekiguchi H, Hassan H. Performance of new hybrid heat sink with trimmed fins and microchannels for thermal control of a triple-junction concentrator photovoltaic cell. Appl Therm Eng 2024;252. https://doi.org/10.1016/j.applthermaleng.2024.123695.

[16] 3C44A – with 10×10 mm2Concentrator Triple Junction Solar cell. http://www. azurspace.com 2016:1–6.

[17] Aldossary A, Mahmoud S, Al-Dadah R. Technical feasibility study of passive and active cooling for concentrator PV in harsh environment. Appl Therm Eng 2016;100:490–500. https://doi.org/10.1016/j.applthermaleng.2016.02.023.

[18] Hasan O, Arif AFM, Siddiqui MU. Finite element modeling, analysis, and life prediction of photovoltaic modules. J Sol Energy Eng Trans ASME 2014;136. https://doi.org/10.1115/1.4026037.

[19] Ahmed M, Radwan A. Performance evaluation of new modified low-concentrator polycrystalline silicon photovoltaic/thermal systems. Energy Convers Manag 2017;149:593–607. https://doi.org/10.1016/j.enconman.2017.07.057.

[20] Zimmermann S, Helmers H, Tiwari MK, Paredes S, Michel B, Wiesenfarth M, et al. A high-efficiency hybrid high-concentration photovoltaic system. Int J Heat Mass Transf 2015;89:514–21. https://doi.org/10.1016/j.ijheatmasstransfer.2015.04.068.

[21] Evola G, Marletta L. Exergy and thermoeconomic optimization of a water-cooled glazed hybrid photovoltaic/thermal (PVT) collector. Sol Energy 2014;107:12–25. https://doi.org/10.1016/j.solener.2014.05.041.

[22] Evans AG, Hutchinson JW. The thermomechanical integrity of thin films and multilayers. Acta Metall Mater 1995;43:2507–30. https://doi.org/10.1016/0956-7151(94)00444-M.

[23] Affecting F, Stress T, Materials C. Factors Affecting Thermal Stress Resistance. J Am Ceram Soc 1953;61:13.

[24] Souare PM, Sylvestre J. Thermal and mechanical analysis of a concentrated photovoltaic module with integrated secondary optics. AIP Conf Proc 2016;1766. https://doi.org/10.1063/1.4962114.